# Interscale energy transfer in the merger of wakes of a multiscale array of rectangular cylinders

Pawel Baj* and Oliver R. H. Buxton
*Imperial College London, Exhibition Road, London SW7 2AZ, United Kingdom*
(Received 25 August 2017; published 27 November 2017)

The near wake of a flow past a multiscale array of bars is studied by means of particle image velocimetry (PIV). The aim of this research is to understand the nature of multiscale flows, where multiple coherent motions of nonuniform sizes and characteristic frequencies (i.e., sheddings of particular bars in our considered case) interact with each other. The velocity fields acquired from the experiments are triple decomposed into their mean, a number of coherent fluctuations, and their stochastic part according to a triple decomposition technique introduced recently by Baj *et al.*, Phys. Fluids **27**, 075104 (2015). This nonstandard approach allows us to monitor the interactions between different coherent fluctuations representative of sheddings of the particular bars. Further, additional equations governing the kinetic energy of the recognized velocity components are derived to provide better insight into the dynamics of these interactions. Interestingly, apart from the coherent fluctuations associated with sheddings, some additional, secondary coherent fluctuations are also recognized. These seem to appear as a result of nonlinear triadic interactions between the primary shedding modes when the two shedding structures of different characteristic frequencies are in close proximity to one another. The secondary coherent motions are almost exclusively supplied with energy by the primary coherent motions, whereas the latter are driven by the mean flow. It is also found that the coherent fluctuations play an important role in exciting the stochastic fluctuations, as the energy is not fed to the stochastic fluctuations directly from the mean flow but rather through the coherent modes.

DOI: 10.1103/PhysRevFluids.2.114607

## I. INTRODUCTION

Turbulent flows are intrinsically multiscale, e.g., the atmospheric boundary layer comprises a broad spectrum of scales of motion, ranging from millimeters (the flow past a grass leaf) up to thousands of kilometers (trade winds). In many cases, turbulence is triggered at a number of length scales simultaneously (e.g., flows through a forest or cityscape). It is reasonable to expect that at each of these levels some sort of flow regularization is enforced, resulting in a certain coherence being introduced into the flow on top of the stochastic turbulent motion. In this regard, features of single- and multiscale generated turbulence can diverge as the former lacks the dynamical interplay of the embedded multiscale coherent motions. The exact importance of these coherent dynamics is not well recognized yet; however, some phenomena observed in natural flows (e.g., the astonishingly quick propagation of wild fires) suggest that it might be of great importance.

The past decade has brought considerable advancement in this matter. Multiscale generated turbulence (or fractal generated turbulence, which is a subset of the latter) was discussed in a theoretical context in, e.g., Refs. [1,2]. On the other hand, practical applications of such flows in different fields were studied as well, e.g., in heat transfer [3], combustion [4,5], wind energy [6], and mixing [7]. The current work, inspired by the aforementioned research, focuses on the near wake of a simple, yet multiscale, array of obstacles. In particular, the flow past an array of bars of nonuniform thickness, which might be called a canonical example of multiscale generated turbulence, is interrogated with a strong emphasis on its dynamical properties. A set of particle image

*p.baj@imperial.ac.uk

 

velocimetry (PIV) experiments was carried out in order to provide data for this analysis. The aim is to isolate features of multiscale generated turbulence at its early stage, as these might be constitutive for its further development, and to achieve a certain level of understanding of the physics of the multiscale generated turbulence by investigating the underlying dynamics.

As the focus of this research is on the near wake, it is expected that a considerable part of the fluctuations' energy is going to be associated with vortex shedding. In order to properly acknowledge the existence of this coherent motion, a triple decomposition of the fluctuating velocity field is embraced instead of a classical Reynolds decomposition, as originally proposed in Ref. [8]. Therefore, the total velocity field $\mathbf{u}$ shall be represented as $\mathbf{u} = \bar{\mathbf{u}} + \mathbf{u}' = \bar{\mathbf{u}} + \tilde{\mathbf{u}} + \mathbf{u}''$, where $\bar{\mathbf{u}}$ and $\mathbf{u}'$ denote temporal mean and fluctuations of the velocity field. The latter is further decomposed into its coherent part $\tilde{\mathbf{u}}$ and the remaining stochastic fluctuations $\mathbf{u}''$. While the Reynolds decomposition is straightforward, the triple decomposition requires a technique for discriminating between coherent and stochastic fluctuations. A number of different methods have been proposed in the past to address this problem. To name a few, researchers have used conditional sampling (e.g., Ref. [8]), bin averaging (e.g., Refs. [9,10]), proper orthogonal decomposition-based techniques (e.g., Ref. [11]), and even more complex techniques (e.g., Ref. [12]), among many others. The particular conditions of the current work, however, limit the choice. The main constraints are as follows: There are several different coherent fluctuations involved in the multiscale flow (i.e., shedding of particular bars), the energy associated with particular motions varies significantly (due to nonuniform thickness), and there is no external phase information. A recent method proposed in Ref. [13] was shown to overcome the above difficulties. The method is extensively validated against other triple decomposition techniques in Ref. [13] and the validation is based on data acquired from a very similar setup, which makes it convenient to utilize in the context of the present study.

As mentioned above, the dynamics of the considered flow are the primary interest and thus the kinetic energy budget is investigated. Since a triple decomposition is utilized, it is natural to consider energies of the mean, coherent, and stochastic motions separately. Suitable turbulent kinetic energy budget equations have already been formulated in Ref. [8]; however, they were derived in the context of a single coherent motion, e.g., in the wake of a single cylinder or prism. Since we consider a number of simultaneous coherent fluctuations, a new, suitable form of these equations is derived and further applied to the analysis of the gathered data. This approach is similar to an intermodal energy flow study presented in Ref. [14] (an energy exchange between a number of proper orthogonal decomposition modes, POD, is considered therein) or, more recently, in Ref. [15] (an energy exchange between a slowly varying base flow; the first and the second harmonics of a wall-mounted pyramid's shedding are studied).

Let us briefly present the outline of the present work. Section II describes the experimental setup and quantifies the uncertainty of the experimental data. Section III presents basic characteristics of the flow in the context of both large- and small-scale motion. It also discusses the appearance of the secondary spectral peaks in the power spectral density (PSD) functions of the velocity fluctuations, which had not been well described in the literature until now. Section IV introduces the triple decomposition technique utilized hereafter and applies it to our considered experimental data. Section V focuses on deriving the energy budgets' equations and presenting the associated results. The final section, VI, summarizes our results, discusses them, and presents the conclusions. Some additional information is provided in appendixes for the sake of completeness. These expand discussions of some specific issues raised in the main body of this work (e.g., a validation of certain assumptions).

## II. EXPERIMENTAL SETUP

The experimental campaign, which consisted of four separate experiments, was carried out in the open water channel facility of the Department of Aeronautics at Imperial College London. The cross section of the channel had a size of $600 \times 600$ mm, denoted $H \times H$ hereafter. All the measurements were taken at the same inlet velocity $U_\infty$, 0.2 $\mathrm{ms}^{-1}$. The background turbulence intensity $I_T$ was found (in an auxiliary experiment) not to exceed 1.9% in the bulk flow [see the profile in Fig. 1(a);

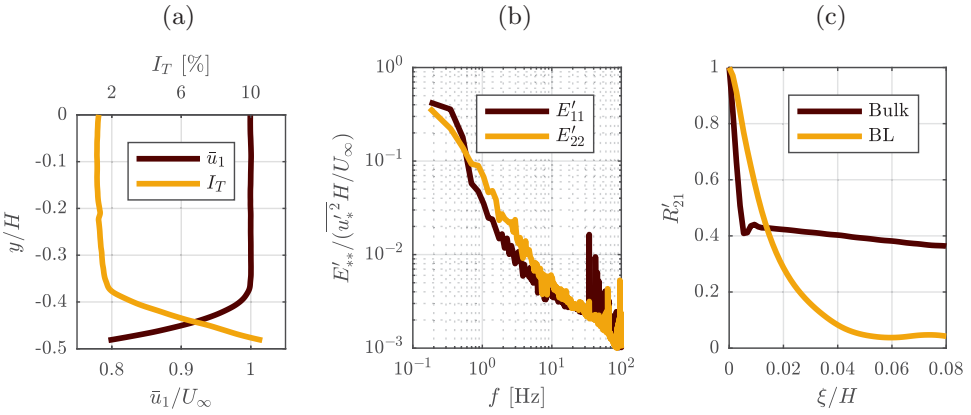


FIG. 1. Characterization of the free stream at the center plane: (a) the mean streamwise velocity and the turbulence intensity profiles, (b) PSDs of the streamwise and transverse velocity fluctuations evaluated in the bulk flow, and (c) streamwise correlation functions of the transverse velocity fluctuations evaluated in the bulk flow and at the midheight of the boundary layer.

the transverse coordinate $y$ equals 0 at the flumes' center line and $-H/2$ at its floor] and to approach around 12% in the turbulent boundary layer near the flume's floor. The mean streamwise velocity $\bar{u}_1$ profile is also plotted for reference. PSDs of the streamwise and transverse background velocity fluctuations are given in Fig. 1(b) (denoted by $E'_{11}$ and $E'_{22}$, normalized with the respective velocity fluctuations root-mean-square values $u'_1$ and $u'_2$), revealing a relatively large contribution of long waves to the overall fluctuations. The integral length scale of the background turbulence cannot be reliably evaluated. As can be inferred from Fig. 1(c) ($R'_{21}$ denotes the streamwise correlation of the transverse velocity fluctuations and $\xi$ represents a streamwise increment), there is a significant short-distance correlation, associated with the background turbulence, which gets shadowed by a long-distance one, making it impossible to establish the integral length scale. The long-distance correlation likely appears due to some slow variation of the bulk velocity resulting from, e.g., the fluctuating turbulent/nonturbulent interface on all three sidewall boundary layers (leading to acceleration and deceleration of the potential flow), the pump's characteristic, or some other global features. A rough estimate of the integral length scale (evaluated by extrapolating the initial form of the correlation function assuming its exponential trend) returns a value of 4.5 mm (the estimate of the long-distance correlation scale calculated in the same way equals 300 mm). This problem is not present in the boundary layer area, as the turbulence gets stronger [see Fig. 1(c)].

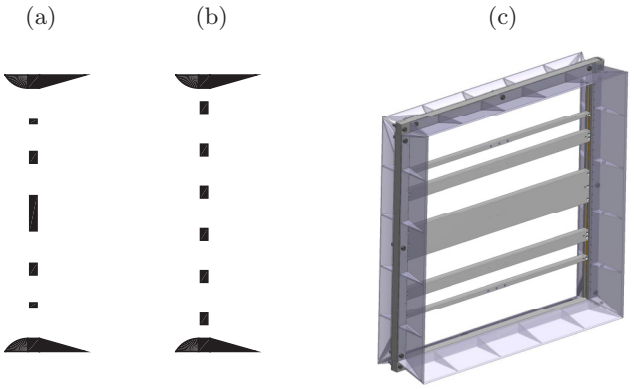


FIG. 2. (a) Multiscale grid, (b) reference uniform grid, and (c) the outer frame.

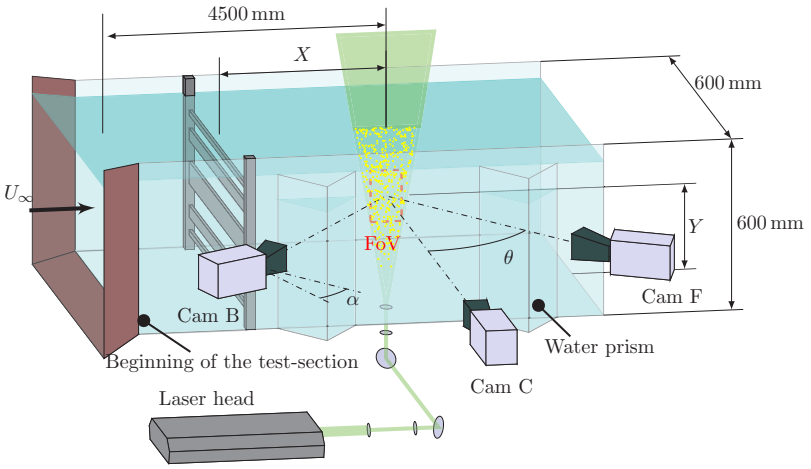


FIG. 3. Schematic of the experimental setup.

Flow past a multiscale bar array [see Fig. 2(a)] was studied in all the experiments. Additionally, a uniform bar array was investigated in some cases in order to provide reference data [see Fig. 2(b)]. The bars were mounted within an outer frame, as shown in Fig. 2(c), which had the the same outer dimension as the channel's cross section. Streamlining elements were attached to the frame in order to minimize its impact on the flow. The blockage was almost the same for both grids and equals 27.9% and 26.7% for the single and multiscale grids respectively based on the frame's inner cross section (the overall blockage, i.e., taking into account the frame as well, reaches 39.6% and 38.6%). The bar thicknesses $t^i$ were equal to 76.2, 25.4, and 9.6 mm for the big, medium, and small bars respectively (they are also referred to as bars I, II, and III throughout the text, the uniform array is constructed only with medium bars) and the streamwise depth was equal to 15 mm. The setup resulted in a global Reynolds number $\mathrm{Re}_H = U_\infty H/\nu = 120\,000$ while the thickness-based Reynolds numbers $\mathrm{Re}_t = U_\infty t/\nu$ fell into an interval 1 900–15 000 ($\nu$ denotes the kinematic viscosity).

Four separate PIV experiments were carried out to characterize different aspects of the flow. A schematic of the setup, given in Fig. 3, applies to all of them. The cameras and other optics were fixed at the same position for all measurements, roughly 4.5 m downstream of the entrance to the flume's test section, and focused at the midplane of the channel. The grid was mounted to a traverse that can adjust its upstream position in order to examine the flow at different locations downstream of the grid.

The difference in the initial conditions that were imposed at different upstream positions of the grid was negligible; i.e., the boundary layer grew by roughly 10% between the grid's extreme positions [its thickness is of the order of 70 mm; see Fig. 1(a)]. Surface waves were not observed during the course of experiments. Moreover, all the measurements were taken below the center line, far from the free surface. Therefore, the potential impact impact of waves is neglected in this work.

A large field of view (FoV) was monitored in experiment 1 with the intention of documenting the large-scale properties of the flow. It consisted of six separate measurements taken at consecutive downstream locations, starting from the frame's rear face (see Fig. 4). The size of the total monitored area, located between the flume's floor and its center line, equaled $300 \times 600$ mm. Experiment 2, on the other hand, provided temporally resolved vertical profiles of the velocity field, which allows spectral analysis of the flow. These were taken at the centers of the particular fields of view of experiment 1 ($x/H = \{0.07, 0.24, 0.41, 0.57, 0.75, 0.91\}$; see Fig. 4). Finally, experiments 3 and 4 were focused on a number of specific regions and provided spatially resolved information in narrow windows, which are centered on $(x/H, y/H) = \{(0.22, -0.34), (0.23, -0.26), (0.23, -0.35), (0.36, -0.37)\}$. Experiment 3 consisted of an additional window centered at $(x/H, y/H) = (0.57, -0.21)$. The small-scale properties of the flow are evaluated based

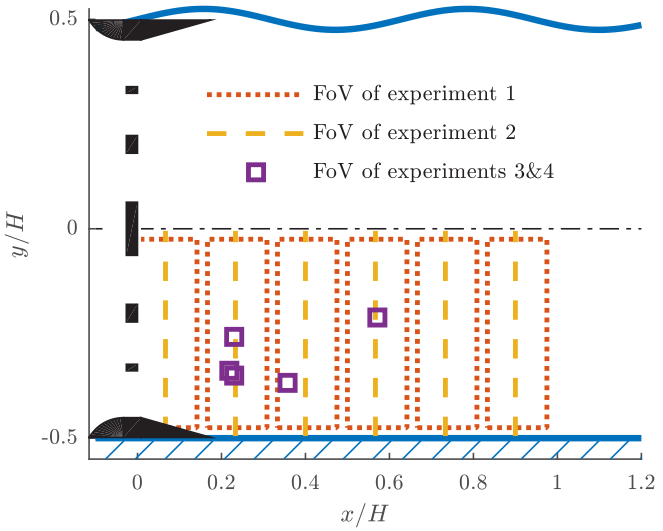


FIG. 4. Locations of the fields of view of particular measurements.

on the data acquired from these two. These exact spots were considered because they coincide spatially with some characteristic features of the flow field (see Secs. III and V for more details).

Two different types of high-speed cameras were used: Phantom Miro M310 and Phantom v641 (providing image resolution of $1280 \times 800$ px and $2560 \times 1600$ px respectively). Two cameras operating simultaneously in a side-by-side arrangement were utilized in experiments 1 and 2 instead of a single camera C, which yielded a larger stitched field of view. The side cameras (i.e., cameras B and F) were only used for the stereoscopic measurements (see Table I for further details). The illumination was provided by a Nd:YLF laser, which ran at a frequency of 500 Hz throughout the experiments, and an optical system that formed a thin diverging laser sheet having a thickness of 0.7 mm.

TABLE I. Summary of the experiments' parameters ($f_{aq}$, $T_{aq}$, $N_{aq}$, $\delta t$, IW, $\Delta_x$ denote respectively acquisition frequency, acquisition time, number of image pairs, time delay between consecutive frames, interrogation window size, and spatial resolution).

| | Experiment 1 | Experiment 2 | Experiment 3 | Experiment 4 |
|---|---|---|---|---|
| Type | 2C-2D PIV<br>Large FoV | 2C-2D PIV<br>Time-resolved | 3C-2D PIV<br>Stereo PIV | 2C-2D PIV<br>High spatial resolution |
| Cam C | 2×Phantom Miro M310<br>2×Sigma 70 mm f/2.8 | 2×Phantom Miro M310<br>2×Sigma 70 mm f/2.8 | Phantom v641<br>Nikon 135 mm f/2 | Phantom v641<br>Sigma 180 mm f/2.8 |
| Cams B&F | Disabled | Disabled | Phantom v641<br>Nikon 135 mm f/2 | Disabled |
| $f_{aq}$ [Hz] | 25 | 500 | 100 | 100 |
| $T_{aq}$ [s] | 90 | 120 | 150 | 300 |
| $N_{aq}$ [–] | 2 250 | 60 000 | 15 000 | 30 000 |
| $\delta t$ [ms] | 4.6–6.6 | n/a | 1.25 | 0.56 |
| IW [px] | 16 | 16 | 24 | 24 |
| Overlap [%] | 75 | 75 | 50 | 50 |
| FoV size $(x \times y)$ [mm] | $100 \times 300$ | $8 \times 300$ | $15 \times 15$ | $10 \times 10$ |
| $\Delta_x$ [mm] | 2.10 | 2.10 | 0.64 | 0.33 |

Experiment 3 provided stereoscopic PIV measurements. The angular displacement method (see Ref. [16] for reference) was used with the lines-of-sight divergence half-angle $\theta$ (see Fig. 3) equal to 45°, which guarantees uniform measurement error across all velocity components (as suggested by Ref. [17]). Auxiliary water prisms were mounted in front of cameras B and F to ensure their optical axes were perpendicular to the air-water interface. Additionally, the Scheimpflug deflection angle $\alpha$ was applied between the cameras and their respective lenses in order to yield properly focused images. Camera C was operated simultaneously to the two others; however, its recordings were not part of the stereo measurement. Instead, it provided an overview of planar velocity within a larger field of view (similar to the one of experiment 1). Note that the results of this measurement are not shown in this paper explicitly; rather they are used as a reference for conditional averaging of the stereo measurement (this is further discussed in Sec. IV). A set of nine calibration images was collected before each measurement. A plain, dotted board (dots' spacing equals 2.5 mm) was used as the calibration target, which was traversed across the thickness of the laser sheet with a step size of 0.15 mm. A third-order polynomial was used as the mapping function in the calibration process, which yielded a fit's standard deviation of less than 0.01 px.

The flow was seeded with polyamide particles during experiments 1 and 2 and with borosilicate glass particles for experiments 3 and 4, having an averaged diameter of 7 and 11 $\mu$m respectively (specific gravity equals 1.1 for both). The Stokes-flow-based approximation of the particles response time $\tau_p$ was found to be equal to roughly 7.5 $\mu$s for the larger particles. Under an assumption that the Kolmogorov length scale equals 0.1 mm, which is a conservative estimate based on Ref. [18], which used a similar facility, one can evaluate the Kolmogorov time scale $\tau_\eta$ to be 10 ms. Therefore, the particle Stokes number $\mathrm{St}_p = \tau_p\,\tau_\eta^{-1} = 7.5 \times 10^{-4} \ll 1$ which indicates that the particles followed the smallest scales of motion reliably.

The basic settings of the particular measurements are summarized in Table I. The sizes of respective interrogation windows were chosen to ensure sufficient particle density, i.e., at least 10 particles per window in the cases of experiments 1 and 2 and at least 6 particles per window in the remaining two (this is in line with the practices suggested in Ref. [17]). The time delays between consecutive exposures were established in preliminary checks to allow sufficient averaged particles displacements of at least a quarter of the respective interrogation window size. In the case of stereo PIV (i.e., experiment 3), the out-of-plane displacement was also quantified. Given that the standard deviation of the out-of-plane velocity fluctuations observed in the experiment does not exceed 55 mm s$^{-1}$, 95% of out-of-plane displacements are expected to be smaller than 0.13 mm (the mean out-of-plane velocity is negligible at the midplane considered), which is less than a quarter of the light sheet thickness, producing reliable stereo PIV measurements (see Ref. [19]). It was verified that the gathered data do not suffer from peak locking. As a result of the assumed time separation between consecutive frames, 95% of the instantaneous displacement gradients observed in the particular experiments were smaller than 0.14, 0.06, 0.05, and 0.02 px/px for experiments 1, 2, 3, and 4. This respectively results in the displacement evaluation uncertainty of 0.3, 0.11, 0.10, and 0.07 px (following Ref. [17]). These values (except for the first one) are of order of the PIV uncertainty floor of 0.06 px suggested by Ref. [20]; thus their effect on the total uncertainty of the present measurements should be limited.

Commercial PIV software (DAVIS, LaVision) was used in the course of data postprocessing for the evaluation of the instantaneous velocity fields. A multipass correlation method was applied (the parameters for particular experiments are displayed in Table I). A Gaussian fitting was used for subpixel interpolation. A median filter was applied to filter out spurious vectors (the filter's size was set to $5 \times 5$). The minimum peak ratio (ratio of the primary and secondary correlation peaks) was kept above 1.2 (otherwise the vector was removed). The missing vectors were further interpolated. In all cases, the number of replaced vectors was limited to 3% of the total number (excluding the outer frame of two rows of vectors). A self-calibration algorithm (see Ref. [21] for details) was utilized in the case of the stereoscopic data to improve the calibration. The final stereo reconstruction error was less than 0.45 px in 95% of cases, which is below the threshold of 0.5 px suggested in Ref. [17]. All the additional postprocessing was done with dedicated in-house codes.

TABLE II. Relative measurement error $e'_{\mathrm{rms}}/u'_{\mathrm{rms}}$ [%]. For experiments 1 and 2, bounds of the error are within the respective fields of view.

| $x/H$ | 0.07 | 0.24 | 0.41 | 0.57 | 0.75 | 0.91 |
|---|---|---|---|---|---|---|
| | | | $e'_{\mathrm{rms}}$ [px] | | | |
| Experiment 1 | 0.07–0.24 | 0.07–0.13 | 0.06–0.10 | 0.08 | 0.08 | 0.08 |
| Experiment 2 | 0.07–0.31 | 0.08–0.13 | 0.09–0.11 | 0.10 | 0.10 | 0.10 |
| Experiment 3 | | | 0.09 | | | |
| Experiment 4 | | | 0.13 | | | |
| | | | $e'_{\mathrm{rms}}/u'_{\mathrm{rms}}$ [%] | | | |
| Experiment 1 | 2–14 | 3–10 | 2–7 | 2–6 | 2–6 | 2–6 |
| Experiment 2 | 5–18 | 4–10 | 3–8 | 2–9 | 2–9 | 2–9 |
| Experiment 3 | | | 3 | | | |
| Experiment 4 | | | 5 | | | |

The uncertainty of a particular PIV measurement arises from unpaired particles due to the out-of-plane motion, large in-plane displacement (relatively to the interrogation window size), nonuniformity of the seeding density or the illumination, considerable velocity gradients across the interrogation window, thermal noise of the camera's sensor, etc. It is hard to establish the exact contribution of these particular error sources in a practical situation. However, the cumulative uncertainty can be conservatively quantified by comparing single-point velocity variance with the extrapolation of the velocity correlation evaluated at zero displacement (see Ref. [22]). Its measure, expressed as a rms value of the measurements' random error $e$, is checked for each individual experiment at all the considered locations. The results are summarized in Table II. The high relative error of experiments 1 and 2, appearing at the initial measurement positions, is associated with a fast, laminar flow which exists near the flume's floor [see Fig. 5(a) in the following section]. The

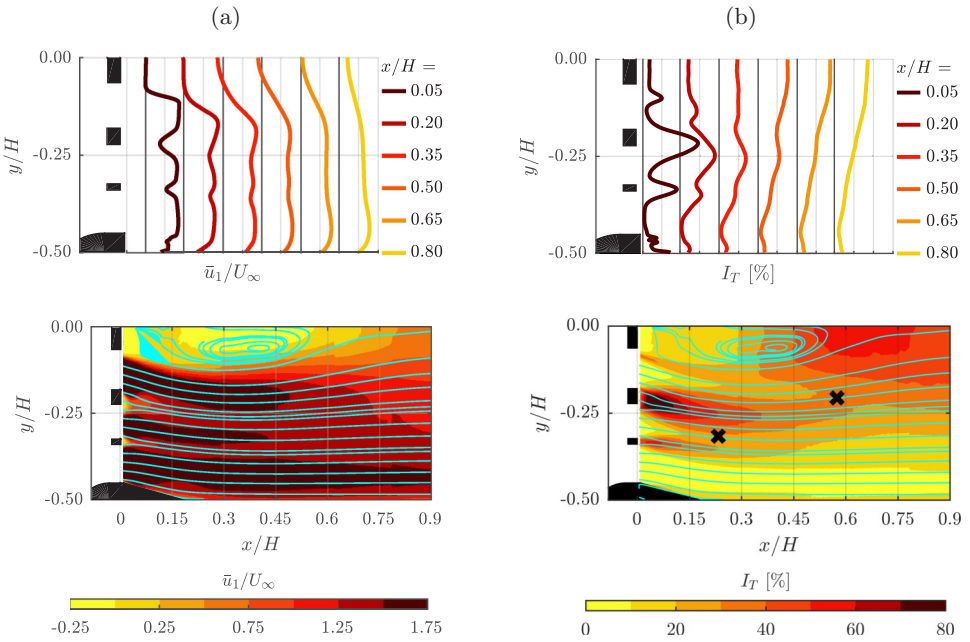


FIG. 5. Transverse profiles and stitched fields of view for experiment 1: (a) mean streamwise velocity and (b) fluctuations intensity (wakes' intersection points are marked with crosses, based on experiment 1).

TABLE III. Critical measures of data convergence evaluated for different experiments and positions: number of independent measurements ($T_{aq}/T_0$) and widths of 95% confidence intervals for basic velocity statistics.

| $x/H$ | | 0.07 | 0.24 | 0.41 | 0.57 | 0.75 | 0.91 |
|---|---|---|---|---|---|---|---|
| $T_{aq}/T_0$ | Exp. 1 | 581 | 468 | 349 | 345 | 438 | 506 |
| | Exp. 2 | 775 | 624 | 465 | 460 | 584 | 674 |
| | Exp. 3 | | | 575 | | | |
| | Exp. 4 | | | 1150 | | | |
| $\pm\frac{\delta\bar{u}_i}{\sqrt{\overline{u_i'^2}}}$ [%] | Exp. 1 | 8.1 | 9.1 | 10.5 | 10.6 | 9.4 | 8.7 |
| | Exp. 2 | 7.1 | 7.9 | 9.1 | 9.2 | 8.1 | 7.6 |
| | Exp. 3 | | | 8.2 | | | |
| | Exp. 4 | | | 5.8 | | | |
| $\pm\frac{\delta\overline{u_i'^2}}{\overline{u_i'^2}}$ [%] | Exp. 1 | 11.6 | 12.8 | 15.0 | 15.0 | 13.4 | 12.2 |
| | Exp. 2 | 10.0 | 11.2 | 13.0 | 13.0 | 11.6 | 10.8 |
| | Exp. 3 | | | 11.6 | | | |
| | Exp. 4 | | | 8.2 | | | |
| $\pm\frac{\delta\overline{(\partial u_i'/\partial x_k)^2}}{\overline{u_i'^2}/\Delta_x^2}$ [%] | Exp. 1 | 23.2 | 25.6 | 30.0 | 30.0 | 26.8 | 24.4 |
| | Exp. 2 | 20.1 | 22.4 | 26.1 | 26.0 | 23.2 | 21.6 |
| | Exp. 3 | | | 23.2 | | | |
| | Exp. 4 | | | 16.4 | | | |

time separation between PIV exposures was optimized to better resolve the wake areas; hence, the error decreases there (note that at the furthest downstream stations the mean velocity is much more uniform and hence so is the error), whereas it can be considerable elsewhere. The absolute error, on the other hand, peaks in the wake areas, where high instantaneous velocity gradients are present. In the case of experiments 3 and 4, the error is uniform across all measurement positions and of order of the lower bounds of the former two.

An assessment of convergence of velocity statistics requires establishing numbers of independent samples acquired in each experiment. It was assumed that the number of independent samples can be approximated by $T_{aq}/T_0$, where $T_0$ is the integral time scale $T_0$, i.e., an integral of temporal correlations of streamwise velocity. $T_0$ was evaluated for each experiment at every measurement station; its values are summarized in Table III. Note that in each case $T_{aq}/T_0$ is sufficiently high (i.e., $>30$), which allows usage of the central limit theorem for evaluating uncertainty of the velocity statistics. Formulas listed in Ref. [23] were used for this purpose. The half-widths of 95% confidence intervals for the most important statistics, i.e., $\bar{u}_i$, $\overline{u_i'^2}$ and $\overline{(\partial u_i'/\partial x_k)^2}$, are reported in Table III (the critical values observed in particular FOVs are presented). Only normal components of the Reynolds stresses and of the velocity derivatives correlation tensor are considered there for the sake of brevity. The uncertainty of the shear components accounted for 50–80% of the corresponding normal components. Note that there is also additional bias error due to the noise self-correlation involved in the normal components' measurements. This, however, accounted for less than an order of magnitude smaller contribution and is neglected here.

## III. GENERAL FLOW CHARACTERISTICS

### A. Large-scale properties

Let us start with a characterization of some global properties of the flow. The mean streamwise velocity and fluctuation intensity fields are shown in Fig. 5. The flow consists of five wakes of

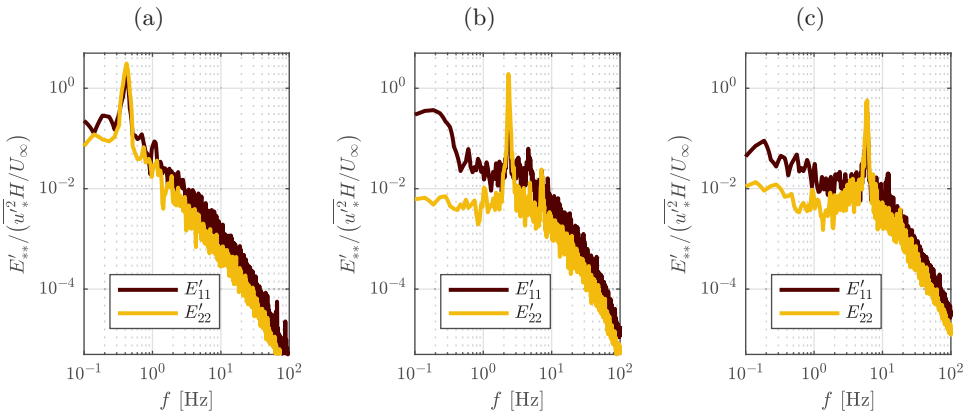


FIG. 6. PSDs of streamwise and transverse velocity components measured at the center line of (a) wake I ($x/H = 0.57$), (b) wake II ($x/H = 0.07$), and (c) wake III ($x/H = 0.07$, based on experiment 2).

particular bars that are relatively distinguishable (only three wakes are captured within the field of view). The wakes of the medium and smallest bars appear to be deflected outward from the center line. The fluctuation intensity field allows a convenient definition of the adjacent wakes' intersection point. Let us denote with this term a point located between two neighboring wakes, where the spatial gradient of the fluctuations intensity field vanishes. Two such points are marked in Fig. 5(b) at the respective downstream positions of $x/H = 0.23$ and $x/H = 0.57$. Note that the distance between a grid and the expected wakes' intersection point proved to be a crucial parameter for the description of fractal-generated turbulence (see Refs. [24] or [18] for reference). Note also that one of the spots considered in experiments 3 and 4, i.e., $(x/H, y/H) = (0.22, -0.34)$, is located in the vicinity of the upstream intersection point, while two other considered spots, i.e., $(x/H, y/H) = \{(0.23, -0.26), (0.23, -0.35))\}$, correspond to maxima of fluctuations intensity within the small and the medium wakes evaluated at the downstream position of their respective intersection points.

The thickest bar creates an elongated recirculation area whose streamwise extent exceeds $5t^I$. This is significantly more than when compared to the standalone bar case usually considered in the literature (roughly $1.6t^I$ could be expected for the given aspect ratio based on Ref. [25]) or to the remaining two bars' wakes. A similar observation applies to the peak of fluctuations intensity, which is located at $5.5t^I$. Upstream of this peak, one can easily distinguish a free shear layer separated from the big bar that bounds stagnated fluid behind the bar. The wake of the medium bar appears to be deflected toward the floor and it intersects the big wake roughly at the position of the fluctuations' intensity peak of the big wake. Deflection of the smallest wake is less pronounced but yet it exists. The intersection point of the small and the medium wakes is postponed downstream of the fluctuations' intensity maxima associated with each of them. It is also worth mentioning that a jetlike flow is sustained between the floor and the smallest bar. As a general description, it can be said that the flow is highly inhomogeneous and anisotropic at all considered locations.

Flow past the uniform array is not illustrated here for the sake of brevity; however, it is worth mentioning that it consists of six wakes which are all similar to each other (there is some nonuniformity of the outward wake due to interaction with the boundary layer though). Their intersections occur at almost the same downstream location, equal to $x/H = 0.32$. In general, the flow exhibits milder spatial gradients of the mean velocity field and of the fluctuations intensity field compared to those observed in the flow past the multiscale array at the corresponding downstream location. The gradients tend to vanish more quickly as well.

The basic spectral characteristics of the individual wakes of the flow past the multiscale array can be deduced from Fig. 6 ($E'_{11}$ and $E'_{22}$ denote PSDs of the streamwise and transverse velocity

TABLE IV. Vortex shedding parameters ($A$ denotes the bar cross sections' aspect ratio, i.e., the thickness to streamwise depth ratio, based on experiment 2).

| | Bar I | Bar II | Bar III |
|---|---|---|---|
| $A$ | 5.08 | 1.69 | 0.64 |
| $\mathrm{Re}_t$ | 15 240 | 5 080 | 1 900 |
| $f_{\mathrm{sh}}$ [Hz] | 0.40 | 2.35 | 6.05 |
| St | 0.16 | 0.30 | 0.29 |

fluctuations respectively). Note that a Hann windowing technique was applied to calculate these power spectral densities in order to decrease their spectral leakage. The spectral resolution is therefore decreased to 0.05 Hz. Clear, pronounced shedding peaks can be recognized in the PSDs and affiliated to particular wakes. The shedding frequencies $f_{\mathrm{sh}}$ equal 0.40, 2.35, and 6.05 Hz. The corresponding Strouhal numbers St based on the respective bar thicknesses and $U_\infty$, summarized in Table IV, exhibit considerable scatter and diverge from the values observed for the flow past a single, standalone cylinder ($\mathrm{St} \simeq 0.13$ is reported for a square cylinder at moderate Reynolds numbers in, e.g., Refs. [25–27]; $\mathrm{St} \simeq 0.17$ was observed for a flat plate in Ref. [26]). There are several factors that could be responsible for this result. The scatter might be understood in terms of a deflected gap flow effect (see Refs. [28] or [29] for reference). It has been observed that two bars that stay in proximity might affect each others' shedding in a way that one Strouhal number is decreased while the other increases (reaching values of roughly 0.07 and 0.21 respectively for a sufficiently small gap, as shown by Ref. [28] for a pair of square prisms). The critical gap width that triggers this effect is roughly equal to the diameter of the bigger of the interacting bars. Since a gap between the biggest and the medium bars equals $0.9t^I$; this phenomenon might be effective in our considered flow. Reference [30] showed that shear can significantly alter the Strouhal number of a cylinder's shedding. In particular, a velocity increment of the order of 10% across the bar diameter (which is what is observed in the present study) was shown to increase the Strouhal of a circular cylinder' shedding by 30%. An inclination of the incoming flow can also affect the shedding frequency, as reported in Ref. [31]. An angle of 15° was shown to increase the square prism's shedding Strouhal number by 15%. The inclination of the incoming flow in the present study was roughly estimated to be of order of 15° and 10° for the medium and the small bars, respectively. Last but not least, Ref. [32] reported increasing Strouhal number with increasing blockage. A change in the Strouhal number of 8% was observed by the authors as the blockage rose from 6% to 15%. The blockage in the current study equals roughly 27%. Given the above, the relatively high Strouhal numbers observed in the current study could plausibly be the result of a combination of the listed effects.

Interestingly, the vortex shedding spectral characteristics are not preserved across different experiments, although, as stated in Sec. II, the setup was kept the same for all the measurements (i.e., the flow geometry and the incoming flow velocity). Non-negligible shifts of the observed shedding frequencies exist between particular experiments as indicated in Fig. 7. It is most evident in the case of the smallest bar, which sheds at frequencies of 6.00, 6.05, 5.45, and 5.50 Hz respectively for experiments 1 to 4 ($\max \Delta\mathrm{St} = 0.03$). Similarly, though less pronounced, the shedding frequencies of the medium bar span from 2.20 to 2.35 Hz ($\max \Delta\mathrm{St} = 0.02$). The exact reason for this behavior is unknown; nevertheless, one can consider the bistable characteristics of gap flows as a plausible explanation. As reported by many researchers (e.g., in Refs. [33–35]), a random switching between two stable flow modes occurs in such flows with the time scale considerably larger than the shedding time scale. The mean time between switches has been shown in Ref. [36] to be Reynolds number dependent. Similar phenomena have been observed in the case of a row of multiple cylinders (e.g., Refs. [37,38]); however, the behavior is even more complex. Given the above, quasistable gap flow can be the reason for this observed discrepancy. It is also worth noting that a significant scatter in

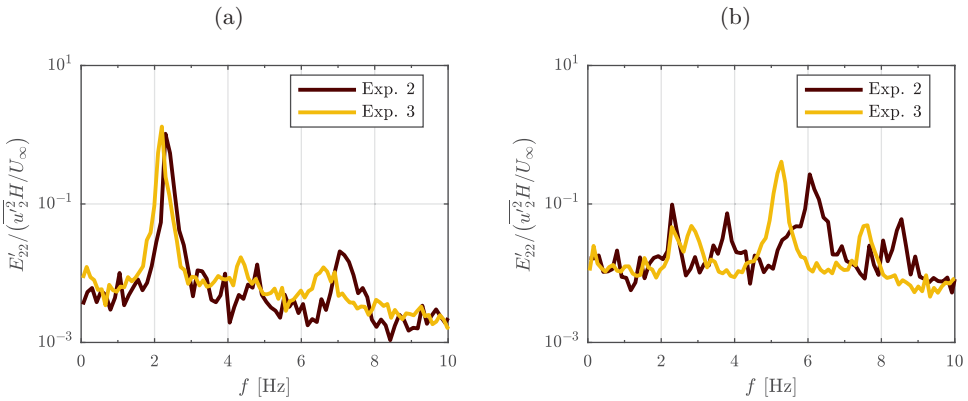


FIG. 7. Shift of the shedding peaks of the transverse velocity PSDs measured in different experiments at the center line of (a) wake II ($x/H = 0.07$) and (b) wake III ($x/H = 0.07$).

the measured shedding frequencies is already reported in the literature for gap-deflected flows. Data presented in, e.g., Refs. [29,33,39] exhibit similar levels of Strouhal number variation to the one present in this work. This scatter is explicitly noted in Ref. [39], simply arguing that there is some variation in the magnitude of the shedding frequencies. Since the focus of this work is elsewhere, this reported observation is to be left aside. Nevertheless, one should bear in mind that some discrepancies between results obtained in different experiments are possible in further assessments.

### B. Small-scale properties

Experiments 3 and 4 give access to the small-scale properties of the velocity fluctuations. It should also be noted that results of the stereoscopic measurements (i.e., experiment 3) are utilized in the study of the turbulence kinetic energy budget, which requires confident evaluation of the instantaneous velocity gradients. It is, therefore, worth validating experiment 3 against experiment 4 as the latter provides better spatial resolution as well as better statistical convergence, although its noise level is slightly higher (see Tables II and III).

The measured velocity gradients are sensitive to both spatial resolution and noise level. Note that despite the relatively high spatial resolution of the experiments, the Kolmogorov scale is still under-resolved. Reference [18] reports $\eta$ of approximately 0.14 mm in similar flow conditions, which makes the resolutions of experiments 3 and 4 equal to $4.6\eta$ and $2.3\eta$ accordingly. Reference [40] suggested that a resolution of at least $3\eta$ is required for confident estimation of small-scale quantities, which means that at least the results obtained from experiment 4 should be suitable for the assessment of the small scales.

Table V summarizes the isotropy of the flow at the probed locations. It seems that the flow is far from an isotropic state, both at its large and small scales, as the listed isotropy measures (see Ref. [41] for reference) deviate from unity considerably. Similar values are observed in experiments 3 and 4, except for the quantity $2\overline{(\frac{\partial u_1}{\partial x_1})^2}/\overline{(\frac{\partial u_2}{\partial x_1})^2}$, which is seen to be systematically higher (by roughly 10%) in the planar experiment. These results could have been expected because in a near-wake region the turbulence is not yet well developed. On the other hand, Ref. [42] postulates that local isotropy may not be the most suitable turbulence description in the first place (at least at moderate Reynolds numbers) and proposes locally axisymmetric turbulence instead. This concept is adopted in our further considerations and utilized whenever the turbulent kinetic energy dissipation rate $\epsilon'$ is evaluated. A more detailed discussion of our approach is provided in Appendix A.

Table VI presents the dissipation of turbulent kinetic energy $\epsilon'$, normalized with the turbulent kinetic energy averaged along the transverse direction $k'_x$ (1), the convective time scale $H/U_\infty$ and the associated length scales evaluated in experiments 3 and 4. The aforementioned scales

TABLE V. Measurement of large- and small-scale isotropy (based on experiments 3 and 4).

| $x/H$ | 0.22 | 0.23 | 0.23 | 0.36 |
|---|---|---|---|---|
| $y/H$ | −0.34 | −0.26 | −0.35 | −0.37 |
| | Experiment 3 ($\Delta_x = 0.64$ mm, stereoscopic PIV) | | | |
| $(u_1)_{\mathrm{rms}}/(u_2)_{\mathrm{rms}}$ | 0.83 | 0.59 | 0.79 | 0.83 |
| $(u_3)_{\mathrm{rms}}/(u_2)_{\mathrm{rms}}$ | 0.78 | 0.50 | 0.63 | 0.76 |
| $2\overline{(\frac{\partial u_1}{\partial x_1})^2}/\overline{(\frac{\partial u_1}{\partial x_2})^2}$ | 0.96 | 0.96 | 0.97 | 0.89 |
| $2\overline{(\frac{\partial u_1}{\partial x_1})^2}/\overline{(\frac{\partial u_2}{\partial x_1})^2}$ | 1.20 | 1.41 | 1.17 | 1.14 |
| $2\overline{(\frac{\partial u_1}{\partial x_1})^2}/\overline{(\frac{\partial u_3}{\partial x_1})^2}$ | 0.89 | 1.68 | 1.13 | 1.09 |
| | Experiment 4 ($\Delta_x = 0.32$ mm, planar PIV) | | | |
| $(u_1)_{\mathrm{rms}}/(u_2)_{\mathrm{rms}}$ | 0.90 | 0.55 | 0.81 | 0.94 |
| $2\overline{(\frac{\partial u_1}{\partial x_1})^2}/\overline{(\frac{\partial u_1}{\partial x_2})^2}$ | 0.98 | 0.97 | 0.81 | 0.94 |
| $2\overline{(\frac{\partial u_1}{\partial x_1})^2}/\overline{(\frac{\partial u_2}{\partial x_1})^2}$ | 1.38 | 1.28 | 1.27 | 1.30 |

are the largest eddies' length scale $L_0 = k'^{3/2}/\epsilon'$, the Taylor length scale $\lambda = \sqrt{15\nu u'^2_{\mathrm{rms}}/\epsilon'}$ (the isotropic definition is used; the exact definition is not critical to the scope of this work), and the Kolmogorov length scale $\eta = \sqrt[4]{\nu^3/\epsilon'}$. Note that the turbulent kinetic energy is evaluated as $\frac{1}{2}(u_1'^2 + u_2'^2 + u_3'^2)$ in the case of experiment 3, whereas it equals $\frac{\alpha}{2}(u_1'^2 + u_2'^2)$ for experiment 4, where $\alpha = (u_1'^2 + u_2'^2 + u_3'^2)/(u_1'^2 + u_2'^2)$, which is calculated based on experiment 3:

$$k'_x = \frac{2}{H}\int_{-H/2}^{0} k'\, dx_2. \tag{1}$$

Despite experiment 4's resolution being twice as good as that of experiment 3, the resolved dissipation rates are similar. There is no clear systematic tendency in the differences. The mean discrepancy

TABLE VI. Turbulent kinetic energy dissipation rate and related scales evaluated based on experiments 3 and 4.

| $x/H$ | 0.22 | 0.23 | 0.23 | 0.36 |
|---|---|---|---|---|
| $y/H$ | −0.34 | −0.26 | −0.35 | −0.37 |
| | Experiment 3 ($\Delta_x = 0.64$ mm, stereoscopic PIV) | | | |
| $\mathrm{Re}_\lambda$ | 184 ± 16 | 268 ± 29 | 165 ± 15 | 122 ± 14 |
| $\epsilon'/(k'_x U_\infty/H)$ | 6.70 ± 0.65 | 5.99 ± 0.70 | 4.74 ± 0.44 | 1.51 ± 0.17 |
| $L_0$ [mm] | 51.0 ± 8.7 | 111.3 ± 21.1 | 54.5 ± 9.1 | 43.6 ± 8.7 |
| $\lambda$ [mm] | 2.54 ± 0.19 | 3.36 ± 0.28 | 2.75 ± 0.20 | 2.90 ± 0.25 |
| $\eta$ [mm] | 0.101 ± 0.002 | 0.104 ± 0.003 | 0.110 ± 0.003 | 0.134 ± 0.004 |
| $\Delta_x/\eta$ | 6.3 ± 0.2 | 6.1 ± 0.2 | 5.8 ± 0.1 | 4.8 ± 0.1 |
| | Experiment 4 ($\Delta_x = 0.32$ mm, planar PIV) | | | |
| $\epsilon'/(k'_x U_\infty/H)$ | 5.24 ± 0.54 | 6.56 ± 0.75 | 4.52 ± 0.46 | 2.27 ± 0.26 |
| $L_0$ [mm] | 65.3 ± 11.4 | 101.6 ± 19.0 | 57.2 ± 9.9 | 29.1 ± 5.8 |
| $\lambda$ [mm] | 2.87 ± 0.22 | 3.21 ± 0.26 | 2.82 ± 0.21 | 2.37 ± 0.20 |
| $\eta$ [mm] | 0.108 ± 0.003 | 0.102 ± 0.003 | 0.112 ± 0.003 | 0.121 ± 0.003 |
| $\Delta_x/\eta$ | 3.0 ± 0.1 | 3.1 ± 0.1 | 2.9 ± 0.1 | 2.6 ± 0.1 |

across the four measurement stations reaches roughly 15%. It is worth noting that if none of the corrections described in Appendix A were applied, the results of experiment 3 would be systematically lower than those of experiment 4 (by a mean value of 63%). Similar conclusions apply to the flow scales reported in Table VI. Values of the Kolmogorov length scale oscillate in the interval 0.10–0.14 mm, which is in good agreement with Ref. [18]. Local Reynolds numbers $\mathrm{Re}_\lambda$ reach moderate values of 122–268, which are also comparable with those of Ref. [18], showing that, despite the early stage of the flow's evolution, the turbulence is well developed at the probed locations. The resultant resolution of experiment 3 is of the order of $6\eta$, yet the results closely match those of experiment 4, whose resolution is twice as good, proving that the stereoscopic data can be used for the energy budget evaluation in Sec. V.

### C. Secondary spectral peaks

Figure 8 depicts the spatial evolution of the transverse velocity spectra. As indicated by Fig. 6, the flow past the multiscale array consists of relatively energetic coherent motions, i.e., von Karman vortices shed by the bars. Peaks corresponding to particular sheddings have been marked with dark arrows. The shedding of the smallest bar seems to dominate close downstream at $x/H = 0.07$ but decays almost completely once $x/H = 0.41$ is reached. The medium bar's shedding stays active throughout the probed space while the biggest bar's shedding appears effectively at the penultimate station ($x/H = 0.41$).

A closer look at the spatial evolution of the spectra allows identification of additional relatively energetic peaks. Figure 8(b) illustrates two of those, appearing at 3.75 and 8.45 Hz. The lower frequency peak is located below the primary shedding peak of the small bar, at the outer shear layer of its wake, whereas the higher frequency peak takes the opposite location at the inner shear layer. The 3.75-Hz peak is quite persistent as its imprint is still present at the farthest location [Fig. 8(d)], unlike the high-frequency peak which is only present at $x/H = 0.24$. Note also that the former is even more persistent than the fundamental high-frequency shedding mode. The remaining two highlighted features appear in Fig. 8(d) at frequencies of 1.95 and 2.75 Hz. These are less pronounced, although they might be shadowed by the main shedding peak $f_{\mathrm{sh}}^{\mathrm{II}}$ to some extent. Similar to the previous case, the lower frequency peak is shifted to the outer shear layer and the higher frequency one to the inner shear layer of the medium bar's wake. Figure 9 presents these peaks at an even farther downstream location of $x/H = 0.75$, where they would be hard to distinguish if plotted in a logarithmic scale. Despite their relatively small amplitudes, it seems that, as in the previous case, the lower frequency secondary peak exceeds both the primary higher frequency shedding and the other secondary peak. The considered secondary features seem to be exclusive to the flow past the multiscale array, as the reference flow past the uniform array does not exhibit any similar behavior (i.e., only a singular pronounced peak can be distinguished at all at the considered downstream locations; see Fig. 8(e) for an indication).

The frequencies affiliated to these additional peaks seem to coincide with linear combinations of the primary shedding frequencies: $f_{\mathrm{sh}}^{\mathrm{II}} \pm f_{\mathrm{sh}}^{\mathrm{I}}$ and $f_{\mathrm{sh}}^{\mathrm{III}} \pm f_{\mathrm{sh}}^{\mathrm{II}}$. Some small discrepancies that appear can be justified with the adopted frequency resolution or with the fact that considerable widths of the studied spectral peaks cause uncertainty in their frequencies' identification. This hypothesis is supported by the data acquired in all the experiments. In particular, in experiments 3 and 4 the main shedding peaks are shifted toward lower frequencies. The additional peaks are also shifted accordingly as shown in Fig. 10 [or Fig. 7(b)]. The respective frequencies measured in experiment 3 equal 1.80, 2.65, 3.15, and 7.75 Hz. It is also worth noting that the appearance of these additional peaks coincides with the wake intersection points marked on Fig. 5(b) (i.e., $x/H = 0.23, 0.57$).

Observations of similar secondary peaks have been reported in the literature in the past, although without particular attention. Reference [43] documented such behavior in the context of the flow past two circular cylinders in a side-by-side arrangement with a diameter ratio of $d_1/d_2 = 2$. It is worth noting that the authors observed a spatial arrangement of secondary peaks similar to that observed in the present study. Reference [44] also reported the existence of the lower frequency secondary

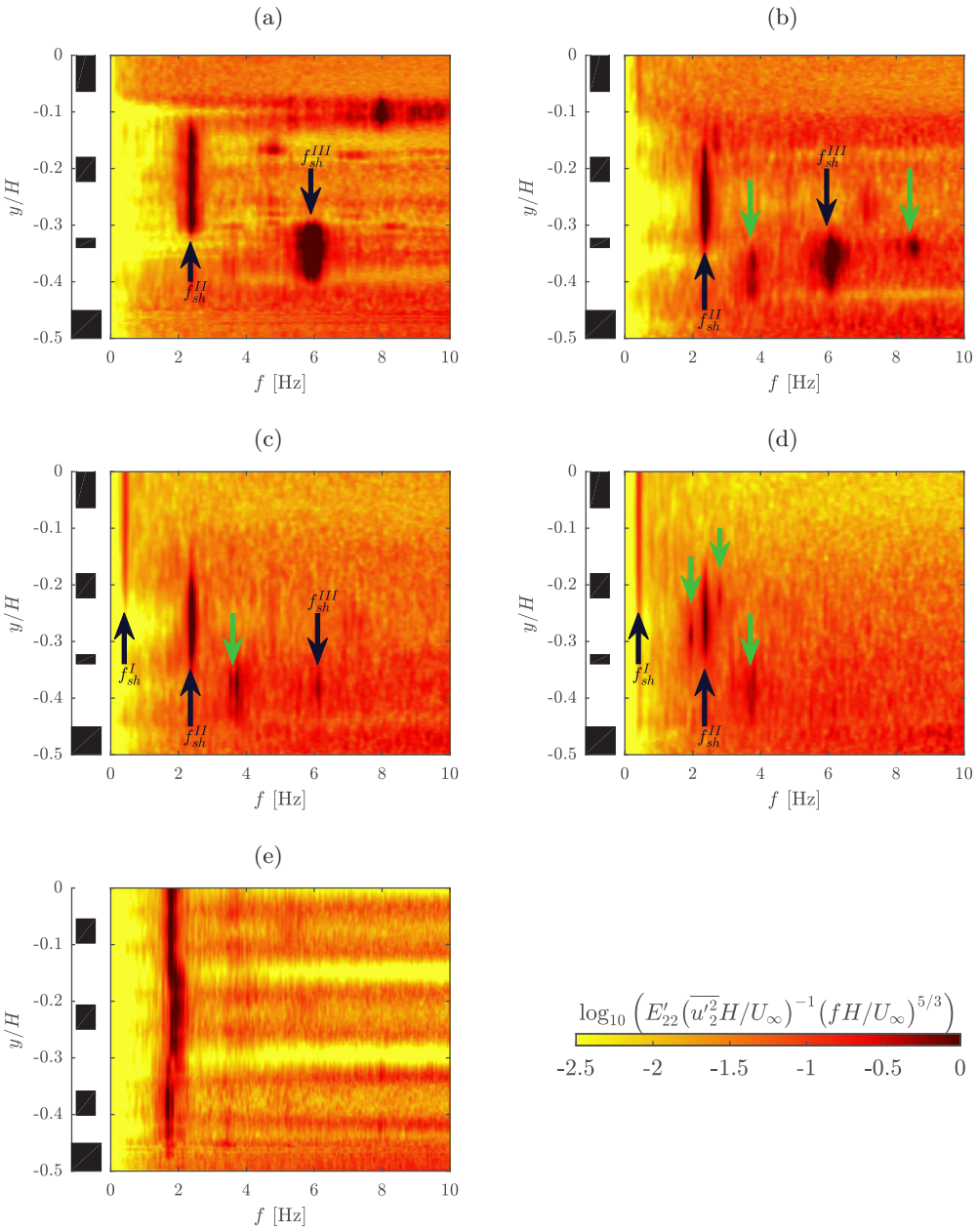


FIG. 8. Compensated PSDs of the transverse velocity component in the flow past the multiscale array at $x/H =$ (a) 0.07, (b) 0.24, (c) 0.41, and (d) 0.57. (e) Compensated PSD of the transverse velocity component in the reference flow past an uniform array at $x/H = 0.07$ (based on experiment 2).

spectral peak, which appears in the context of the flow past two side-by-side circular cylinders with a diameter ratio of $d_1/d_2 = 0.75$ at various gap ratios. The authors speculate that its appearance might be due to a mutual nonlinear interaction between the two wakes. Another example can be found in Ref. [45], who considered the flow past a step cylinder. The additional frequencies that appeared in the flow past the step were associated to certain modulation phenomena.

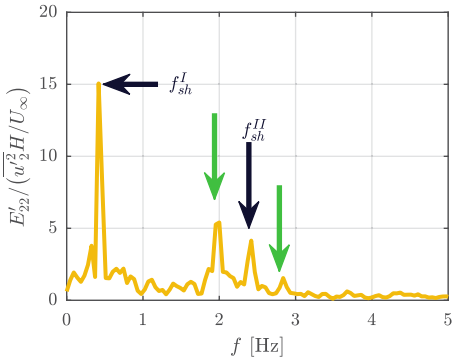


FIG. 9. Appearance of secondary spectral peaks associated with frequencies $f^{\mathrm{II}}_{\mathrm{sh}} - f^{\mathrm{I}}_{\mathrm{sh}}$ and $f^{\mathrm{II}}_{\mathrm{sh}} + f^{\mathrm{I}}_{\mathrm{sh}}$ at $(x/H, y/H) = (0.75, -0.28)$ (based on experiment 2).

Apart from the aforementioned, there is another quite prominent spectral peak that appears at $f \simeq 8.20\,\mathrm{Hz}$ [see Fig. 8(a)]. It can be related to the shear layer that separates from the biggest bar [see Fig. 5(b)], as there is a spatial coincidence of these two. However, this particular peak is of minor importance for the scope of this work.

In summary, the observations given above lead to a conclusion that the interactions of wakes at their early stage of development, where shedding is dominant, undergo a distinctive process that is only effective if the wakes differ in characteristic size or frequency (thus cannot be observed in the reference flow past the uniform array). As two wakes arrive at their intersection point, two additional spectral peaks are induced at the frequencies corresponding to the difference and sum between the primary shedding frequencies. These secondary peaks appear at specific positions with respect to the interacting wakes: The lower frequency peak fixes at the outer shear layer of the smaller of the interacting wakes (outward from the gap between the wakes) while the other locates itself at its inner shear layer. The lower frequency secondary peak is the most persistent. It persists even further downstream than the high-frequency primary shedding peak. The other secondary peak, however, exists only for a relatively short period.

This scenario seems to be reproducible as it is observed in all the experiments considered in this work (despite the reported shedding frequency shifts) as well as in some data from the literature (e.g., Ref. [43]). Although the spectral characterization suggests an ongoing modulation of the

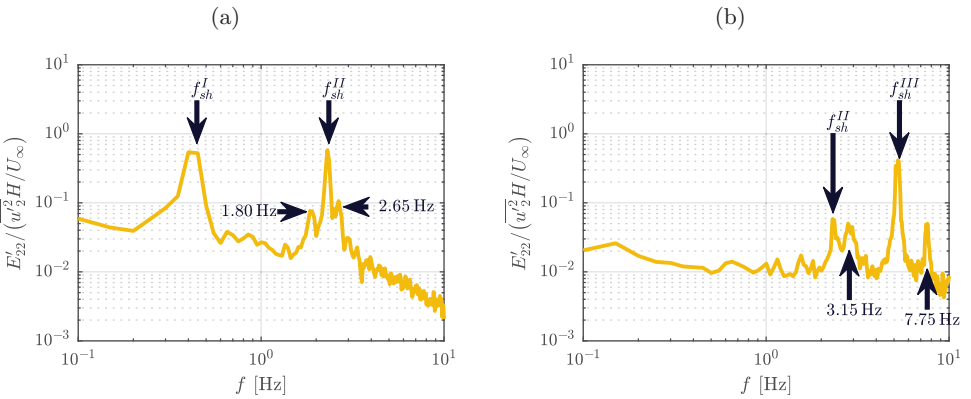


FIG. 10. Characteristic frequencies of the secondary coherent fluctuations at stations: $x/H =$ (a) 0.57 and (b) 0.23 (based on experiment 3).

smaller wake by the bigger one as a plausible explanation, it is puzzling why a specific spatial arrangement of the spectral peak occurs or why the assumed beat frequency is more persistent than the one associated with the shedding. This phenomenon, potentially important for the dynamics of a multiscale flow, deserves closer attention. Motivated by this fact, for the remainder of this work let us focus on characterization of this phenomenon by revealing the underlying velocity field organization and further by considering the energy balance of the flow. Note that in the following sections, for brevity of our notation, all the quantities related to the secondary spectral peaks appear with the appropriate superscripts of II $\pm$ I or III $\pm$ II (while superscripts I, II, and III are affiliated with the respective primary fluctuations).

## IV. TRIPLE DECOMPOSITION

As outlined in the introduction, the velocity fluctuations in our flow consist of both stochastic and coherent parts, which should be treated separately. In particular, the coherent fluctuations associated with individual spectral peaks should be distinguished to aid our understanding of the postulated wakes' interaction phenomenon. This implies that a triple decomposition, as originally proposed in Ref. [8], should be used rather than the traditional Reynolds decomposition. A fluctuating velocity field $\mathbf{u}(\mathbf{x},\tau)$, which is a function of a spatial location $\mathbf{x}$ and time $\tau$, should be treated as a superposition of its temporal mean $\bar{\mathbf{u}}$, coherent fluctuation $\tilde{\mathbf{u}}$, and stochastic fluctuation $\mathbf{u}''$. The triple decomposition method proposed by Ref. [13], which will be employed for this study (see Appendix B for the theoretical background), can further distinguish between a number of different coherent motions $\tilde{\mathbf{u}}^l$, which allows for the accounting of coherent fluctuations associated with different spectral peaks. Thereby, the final triple decomposition definition takes the form of

$$\mathbf{u}(\mathbf{x},\tau) = \bar{\mathbf{u}}(\mathbf{x}) + \sum_l \tilde{\mathbf{u}}^l(\mathbf{x},\tau) + \mathbf{u}''(\mathbf{x},\tau). \tag{2}$$

The adopted triple decomposition method utilizes optimal mode decomposition (OMD; see Ref. [46]) to evaluate velocity modes $\Phi_{\mathrm{OMD}}(\mathbf{x})$ that can be linked to particular coherent fluctuations. These are used to span a basis onto which the total velocity fluctuations are projected. Since the modes are complex, the resultant coefficients are complex numbers as well. After bandpass filtering (see Ref. [13] for an extensive description), their arguments are interpreted as the instantaneous value of the phase $\phi^l$ associated with a given OMD mode while their amplitudes, denoted as $A^l$, are treated as the amplitudes of the respective coherent fluctuations. The final expression for the reconstruction of $\tilde{\mathbf{u}}^l$ is given by Eq. (3) (note that $\underline{*}$ stands for the complex conjugate of $*$):

$$\tilde{\mathbf{u}}^l(\mathbf{x},\tau) = A^l(\tau)\left[\Phi^l_{\mathrm{OMD}}(\mathbf{x})e^{\sqrt{-1}\phi^l(\tau)} + \underline{\Phi}^l_{\mathrm{OMD}}(\mathbf{x})e^{-\sqrt{-1}\phi^l(\tau)}\right]. \tag{3}$$

### A. Extraction of the OMD modes

The method introduced above has been successfully applied to the data gathered in experiments 1–3 (with the exception of station $x/H = 0.57$ of experiment 3). Modes associated with the frequency $f^{\mathrm{I}}$ were recognized for the last four fields of view ($x/H = 0.29$–$0.97$). Frequency $f^{\mathrm{II}}$ was found everywhere except the last field of view ($x/H = 0.00$–$0.80$), while $f^{\mathrm{III}}$ disappears after the first three fields ($x/H = 0.00$–$0.46$). As a rough estimate, the downstream extent of the identified modes is limited by the locations of their corresponding wakes' intersection points, inferred from the fluctuations intensity field [see Fig. 5(b)].

Figure 11 presents the energies and curls of the OMD modes $\Phi_{\mathrm{OMD}}$ corresponding to the highlighted eigenvalues resolved from experiment 1 (i.e., $\Phi_{\mathrm{OMD}} \cdot \underline{\Phi}^T_{\mathrm{OMD}}$ and $|\nabla \times \Phi_{\mathrm{OMD}}|$, the different fields of view are stitched). Blank areas appear as a result of not finding a suitable eigenvalue at several locations. Isophase lines (note that OMD modes are complex) are plotted on top of the curl's contours. Each of the presented modes can be clearly linked to particular wakes as the modes' energies are clearly concentrated within the bounds of different wakes. Note that modes are continuous and smooth across the boundaries of fields of view which suggests

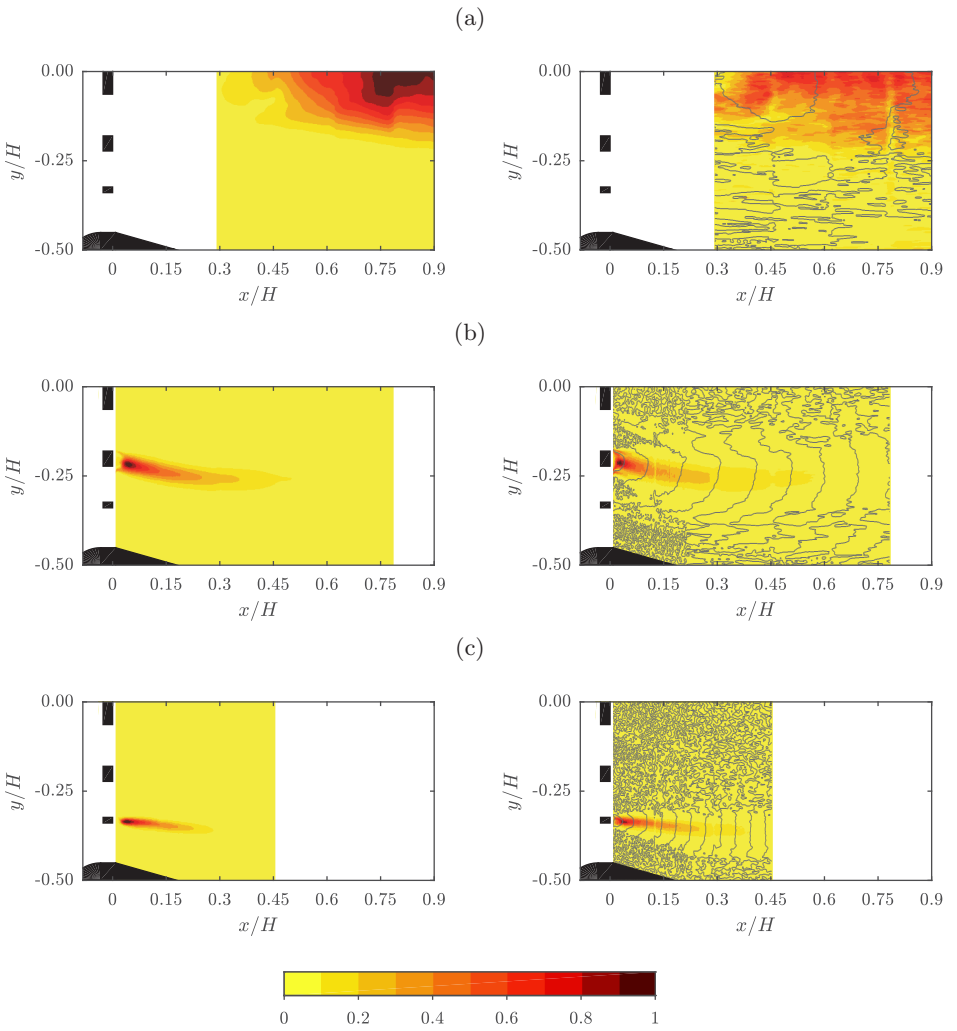


FIG. 11. Energies (i.e., $\Phi_{\mathrm{OMD}} \cdot \underline{\Phi}^{T}_{\mathrm{OMD}}$, left-hand side) and curls (i.e., $|\nabla \times \Phi_{\mathrm{OMD}}|$, right-hand side) of the OMD modes associated with frequencies: (a) $f^{\mathrm{I}}$, (b) $f^{\mathrm{II}}$, and (c) $f^{\mathrm{III}}$; lines denote points of equal curls' phase values (values normalized with their respective maxima, based on experiment 1).

sufficient convergence of the results ($\Phi^{I}_{\mathrm{OMD}}$ is the least smooth which is due to its characteristic low frequency). The topology of the isophase lines clearly demarcates a pronounced spatial area of vorticity coherence (and thus velocity coherence) where the the lines are smooth and continuous, in contrast to their random appearance elsewhere. This is especially clear in Fig. 11(c). Areas associated with different shedding modes overlap to a certain extent; however, the high-vorticity cores are well separated.

The applied triple decomposition procedure also yields similar results for the remaining experiments (these are not presented for brevity). Nevertheless, there were some slight differences in approach to manipulating the data acquired from each experiment which are now documented. In the case of experiment 2, the procedure is nearly the same as described above (and so are the conclusions). However, the high acquisition frequency relative to the observed shedding phenomena would result in much noisier modes (or even prevent them from being detected) if exactly the same approach was to be followed. In order to overcome this issue, in the context of (B1), each instantaneous snapshot

$\mathbf{q}^h$ was compared with $\mathbf{q}^{h+10}$ instead of $\mathbf{q}^{h+1}$ (see Appendix B for details). This guarantees that the change of coherent velocities within the compared snapshot pair is considerably higher than the noise level.

In the case of experiment 3, the data acquired from camera C (see Fig. 3) was merged with the stereoscopic data for the purposes of the OMD analysis. This was necessary because the narrow fields of view of the stereoscopic measurement were not sufficient to enclose all of the coherent motions that occur at their respective downstream locations. Once the OMD was evaluated (i.e., the phase signals for all the sheddings were established), data acquired from camera C was discarded. Similarly to the previous case, snapshots $\mathbf{q}^h$ and $\mathbf{q}^{h+3}$ were compared in the OMD procedure to account for the high acquisition frequency.

### B. Phase averaging

Despite the applied triple decomposition technique being successful in isolating the coherent fluctuations associated with the primary spectral peaks (i.e., vortex shedding modes), it did not offer any access to the modes associated with the secondary peaks recognized in the previous section. Even if the OMD rank $r$ was set to relatively high values (comparable with the total number of snapshots), no clear low-damping peaks would be seen at frequencies affiliated to the secondary peaks. Some other measures were needed to be taken to isolate these fluctuations.

As stated in the introduction, different methods have been used in the past to perform triple decomposition; one of them was phase averaging (e.g., Ref. [9]). The main reason for the previous exclusion of this approach was that no phase reference was available. The authors of Ref. [13] tried to extract a phase reference from a fixed spatial point of a measured velocity field and further use it for conditional averaging but with no success (i.e., conditional statistics established in this way did not present any clear results). The current problem, however, is specific, as the objective is to extract secondary coherent fluctuations associated with frequencies of $f^{l\pm m}$ while the phase reference of both $f^l$ and $f^m$ are known (i.e., phase references of the primary coherent fluctuations). Hence, it can be argued that the missing phase reference of the secondary coherent fluctuations could be expressed as $\phi^l \pm \phi^m$. Let us consider the nonlinear term of the Navier-Stokes equation. As a consequence of distinguishing the primary coherent terms $\tilde{\mathbf{u}}^l$ and $\tilde{\mathbf{u}}^m$ in the first place, the nonlinear term itself should consist of a term $(\tilde{\mathbf{u}}^l \cdot \boldsymbol{\nabla})\tilde{\mathbf{u}}^m$ among others. It is straightforward to show based on (3) that $(\tilde{\mathbf{u}}^l \cdot \boldsymbol{\nabla})\tilde{\mathbf{u}}^m$ is the product of a certain spatial modulation [e.g., $(\Phi^l_{\mathrm{OMD}} \cdot \boldsymbol{\nabla})\Phi^m_{\mathrm{OMD}}$] and a temporal evolution factor $\exp\{\sqrt{-1}[\phi^l(\tau) \pm \phi^m(\tau)]\}$. Under an assumption that this is the driving term of the secondary coherent fluctuations, which seems a plausible scenario, the phase reference of the secondary coherence fluctuation should be equal to $\phi^l \pm \phi^m$, as postulated. Note that a similar idea was also suggested in Ref. [44].

Following the aforementioned logic, let us perform a phase averaging based on $\phi^l \pm \phi^m$. The phase average $\langle a \rangle$ of an arbitrary fluctuating quantity $a$ evaluated for $\phi^l \pm \phi^m = \phi_0$ can be defined as follows:

$$\langle a \rangle = \underset{\phi(\tau)\in G_0}{\mathrm{mean}}\, a(\tau), \tag{4}$$

where $G_0$ is a phase bin bounded by $\phi_0 - \Delta_\phi/2$ and $\phi_0 + \Delta_\phi/2$. The width of the bin is limited on the one hand by the required resolution and by sufficient statistical convergence on the other ($\Delta_\phi$ is set to $\pi/32$ in the following calculations, resulting in 64 bins of roughly 930 images each). Let us express this result in the form of a complex mode (similar to an OMD mode) for convenience. This can be done by taking the normalized second Fourier mode $\Phi_{\mathrm{PA}}$ of the evaluated function $\langle \mathbf{u} \rangle$ (i.e., the second coefficients of the Fourier transform evaluated at each spatial location, which expresses the local amplitudes and phases of waves having wavelength of $2\pi$). Figure 12 provides an example of this process. Figure 12(a) depicts a function $a(y,\tau)$ to be phase averaged based on the associated phase reference $\phi(\tau)$ shown in Fig. 12(b). Figure 12(c) provides the result of this

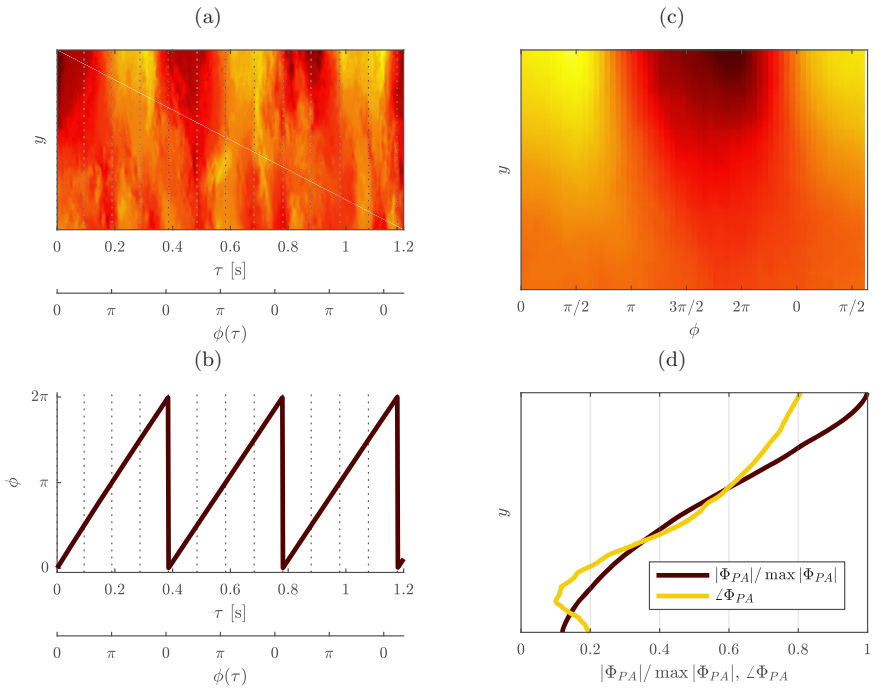


FIG. 12. An example of the Fourier modes extraction: (a) a function $a(y,\tau)$ to be phase averaged, (b) the associated phase reference $\phi(\tau)$, (c) the phase average $\langle a\rangle(y,\phi)$, and (d) the resultant second Fourier mode $\Phi_{\mathrm{PA}}(y)$.

operation, i.e., $\langle a\rangle(y,\phi)$. Finally, Fig. 12(d) presents the final mode $\Phi_{\mathrm{PA}}(y)$, i.e., the second Fourier mode of $\langle a\rangle(y,\phi)$ (the Fourier decomposition is performed along the coordinate $\phi$).

The results of applying this procedure to the data gathered in experiment 1 are presented in Fig. 13 (similar results are observed for the other two experiments). The modes, corresponding to frequencies $f^{\mathrm{II}\pm\mathrm{I}}$ and $f^{\mathrm{III}\pm\mathrm{II}}$, are not as well converged as those of the OMD (see Fig. 11), which is particularly clear for the first pair. This is can be a consequence of the relatively smaller amplitude of these fluctuations as well as of some shortcomings of the utilized technique (i.e., of the underlying assumption about the phase reference). Nevertheless, it is clear that certain structures have been extracted. Along with the previous observations regarding the secondary PSD peaks, the modes affiliated to the higher frequency secondary peaks are mostly located above the center line of the respective primary wake, whereas the ones associated with the lower frequency position themselves below (see Fig. 8). The locations of the maxima of the revealed structures can be confidently measured only for $\Phi_{\mathrm{PA}}^{\mathrm{III}\pm\mathrm{II}}$ (these are marked with circles in Fig. 13). These are equal to $(x/H, y/H) = (0.36, -0.37)$ and $(x/H, y/H) = (0.22, -0.34)$ for $\Phi_{\mathrm{PA}}^{\mathrm{III}-\mathrm{II}}$ and $\Phi_{\mathrm{PA}}^{\mathrm{III}+\mathrm{II}}$ respectively. Note that this coincides with the positions of the two stereoscopic measurements, which is done on purpose (the other two measurements of experiment 3 are located at $x/H$ corresponding to the upstream wakes' intersection point and their transverse positions are set by the locations of the energy maxima of the interacting sheddings). These maxima are considerably postponed compared to the maxima of the corresponding primary modes, which are located close downstream of the bars. The opposite situation is seen in the context of $\Phi_{\mathrm{PA}}^{\mathrm{II}\pm\mathrm{I}}$ as their maxima, despite marginal confidence in their exact locations, occur roughly at the same downstream location as the maximum of energy of $\Phi_{\mathrm{OMD}}^{\mathrm{I}}$. In both cases, however, the wakes' intersection point seems to be representative of the modes' appearance. The isophase lines, also in this case, show pronounced areas of vorticity with

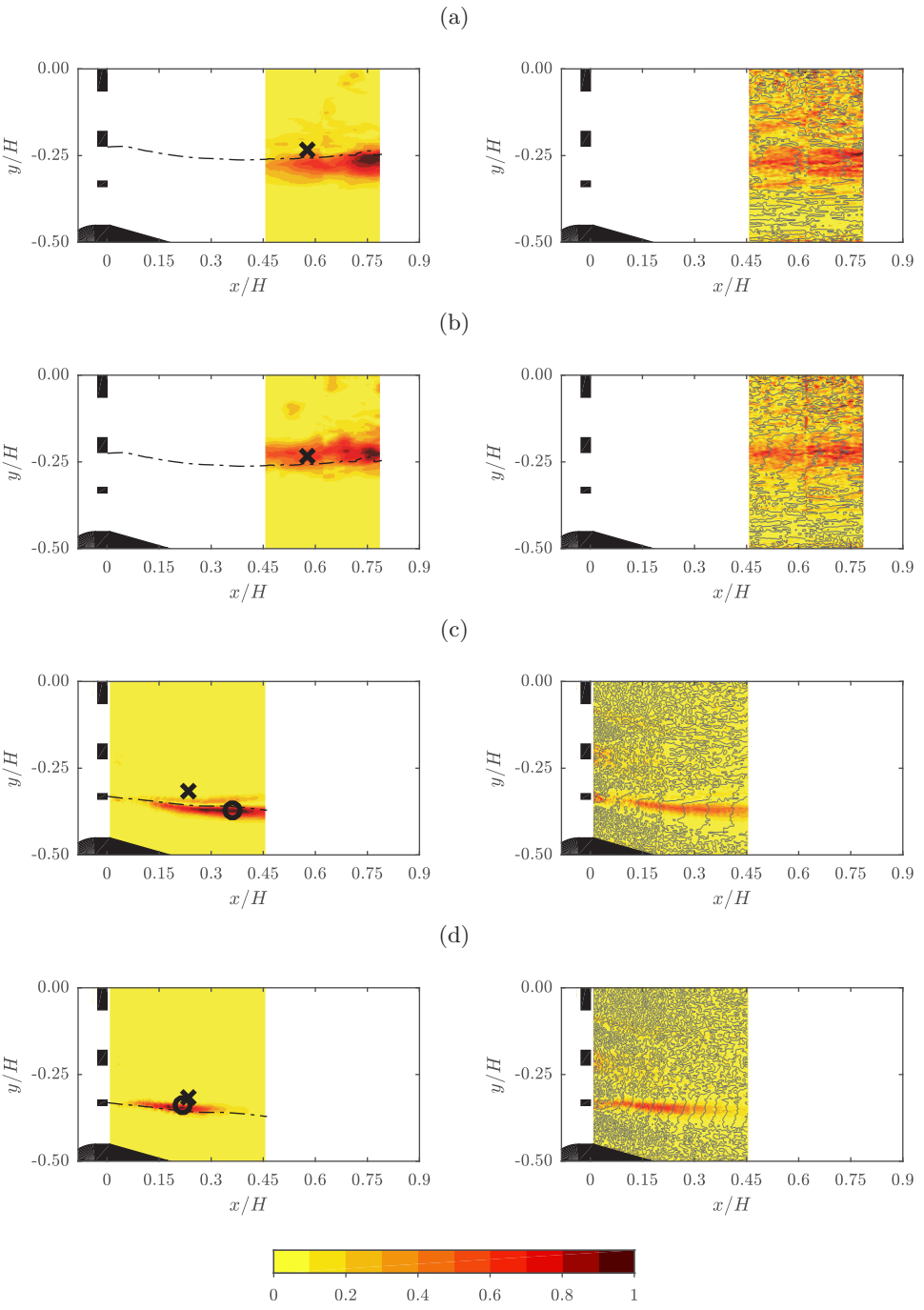


FIG. 13. Energies (i.e., $\Phi_{\mathrm{PA}} \cdot \underline{\Phi}^{T}_{\mathrm{PA}}$, left-hand side) and curls (i.e., $|\nabla \times \Phi_{\mathrm{PA}}|$, right-hand side) of the second Fourier modes of the phase-averaged velocity fluctuations associated with frequencies: (a) $f^{\mathrm{II-I}}$, (b) $f^{\mathrm{II+I}}$, (c) $f^{\mathrm{III-II}}$, and (d) $f^{\mathrm{III+II}}$; continuous lines denote points of equal curls' phase value; dashed lines indicate locations of maxima of amplitude of [(a), (b)] $\tilde{\mathbf{u}}^{\mathrm{II}}$ and [(c), (d)] $\tilde{\mathbf{u}}^{\mathrm{III}}$; crosses designate the wakes' intersection points inferred from the fluctuations intensity field [see Fig. 5(b)]; while circles mark the maximum of the mode's energy field (values normalized with their respective maxima, based on experiment 1).

spatial coherence. However, these areas overlap with the primary wakes' coherence area to a large extent.

So far, a number of complex velocity modes representative of different coherent fluctuations have been identified. These were split into OMD modes (discussed in the previous subsection) and the Fourier modes (discussed in the present subsection) of phase-averaged velocity; however, no further attempt to distinguish between them is made. Hence, the subscripts OMD and PA are dropped in the notation hereafter. The distinguished modes $\Phi^l$ (plus their conjugate pairs) form a projection basis for the evaluation of the respective phase and amplitude signals. Further, (3) can be used for an explicit evaluation of the different components of coherent velocity fluctuations. The results of of the triple decomposition described in this section are briefly discussed in Appendix C in terms of their properties, quality, and reproducibility.

## V. ENERGY BUDGET

### A. Derivation of the energy budget equations

In the traditional approach, the kinetic energy budget of a turbulent flow is split into a part associated with the mean field and one that describes the fluctuations. Each is governed by a separate equation. A different approach was suggested in Ref. [8], which, consistent with the idea of representing fluctuations as a sum of their stochastic and coherent parts, proposed consideration of the kinetic energy of coherent and stochastic fluctuations separately (under an assumption that $\tilde{\mathbf{u}}$ and $\mathbf{u}''$ are uncorrelated) as expressed by (5):

$$k = \tfrac{1}{2}\overline{u_i u_i} = \tfrac{1}{2}\bar{u}_i\bar{u}_i + \tfrac{1}{2}\overline{\tilde{u}_i\tilde{u}_i} + \tfrac{1}{2}\overline{u_i'' u_i''} = \bar{k} + \tilde{k} + k''. \tag{5}$$

The respective governing equations were derived based on the Navier-Stokes equations and auxiliary identities concerning different types of averages. Let us repeat this derivation bearing in mind that the coherent fluctuations may be further split into a number of independent parts. It needs to be noted that the definition of coherent fluctuations utilized in this work [i.e., Eq. (3)] is slightly different than the one used in Ref. [8]:

$$\begin{gathered} c\overline{\bar{a}} = \bar{a}, \quad \overline{\tilde{a}^l} = 0, \quad \overline{a''} = 0, \quad \langle a''\rangle^l = 0, \quad \overline{\langle a\rangle^l} = \bar{a}, \quad \langle\bar{a}\rangle^l = \bar{a}, \\ \begin{cases} \langle\tilde{a}^l\rangle^m \neq 0 & \text{if } f^l = cf^m \\ \langle\tilde{a}^l\rangle^m = 0 & \text{if } f^l \neq cf^m \end{cases}, \quad \overline{\bar{a}\bar{a}} = \bar{a}\bar{a}, \quad \overline{\bar{a}\tilde{a}^l} = 0, \quad \overline{\bar{a}a''} = 0, \\ \begin{cases} \overline{\tilde{a}^l\tilde{a}^m} \neq 0 & \text{if } l = m \\ \overline{\tilde{a}^l\tilde{a}^m} = 0 & \text{if } l \neq m \end{cases}, \quad \overline{\tilde{a}^l a''} = 0, \quad \overline{a''a''} \neq 0. \end{gathered} \tag{6}$$

Let us first introduce a set of identities and assumptions that are to be utilized. These are gathered in (6) ($a$ stands for an arbitrary fluctuating quantity and $c$ is an integer). Note that a symbol $\langle*\rangle^l$ refers to a phase average which is conditioned on the $l$th phase signal (i.e., associated to the $l$th coherent fluctuations). It has to be stressed that in general $\langle\tilde{a}^l\rangle^l \neq \tilde{a}^l$, contrary to what was proposed in Ref. [8]. This is a direct consequence of the fact, that, in accordance with (3), $\tilde{\mathbf{u}}^l$ cannot be expressed purely as a function of a spatial coordinate and phase value as it contains a time-dependent amplitude $A_l$ as a factor. Another important underlying assumption is that the energies of particular coherent fluctuations are well separated in the frequency domain (e.g., their frequency bands do not overlap). As a result, $\langle\tilde{a}^l\rangle^m$ is only nonzero when $\tilde{\mathbf{u}}^l$ equals or is a harmonic of $\tilde{\mathbf{u}}^m$ as well as $\overline{\tilde{a}^l\tilde{a}^m}$ vanishes when $l \neq m$. The remaining relations are rather clear and do not require further comment. A more extensive validation of some of the introduced assumptions can be found in Appendix D.

Before turning to the energy budget, let us consider the incompressible continuity equation $\partial u_i/\partial x_i = 0$. In the case of a classical Reynolds decomposition, it is straightforward to show that it is fulfilled by both the mean velocity field and the fluctuations. It would be convenient to obtain a similar result for the decomposition into stochastic and coherent fluctuations as it would allow us to

express the energy budget in a classical form (i.e., similar to how it is presented in the context of a Reynolds decomposition). To do so, let us consider a phase average of the continuity equation for total velocity fluctuations, given by Eq. (7a), based on an arbitrary phase $\phi^l$:

$$\frac{\partial u_i'}{\partial x_i} = 0. \tag{7a}$$

The right-hand side is surely zero whereas the left-hand side, by applying our assumptions (6), can be reduced to a sum of spatial derivatives of the phase average of the coherent motion $\tilde{\mathbf{u}}^l$ and all its harmonics that are distinguished in the triple decomposition process (the derivatives of the stochastic part vanish as $\langle a'' \rangle^l = 0$), as expressed by (7b):

$$\left\langle \frac{\partial u_i'}{\partial x_i} \right\rangle^l = \sum_m \frac{\partial \langle \tilde{u}_i^m \rangle^l}{\partial x_i} + \frac{\partial \langle u_i'' \rangle^l}{\partial x_i} = \sum_{m: f^m = c \cdot f^l} \frac{\partial \langle \tilde{u}_i^m \rangle^l}{\partial x_i} = 0. \tag{7b}$$

However, if one sets $f^l$ to be the highest distinguished frequency, it cannot have any further harmonics within the considered set of coherent fluctuations and thus the summation reduces to the single term $\partial \langle \tilde{u}_i^l \rangle^l / \partial x_i$. In the next step, one can set $f^l$ to be the second highest coherence frequency. It is possible that, again, this frequency has no harmonic within the distinguished set and the previous reasoning applies. Alternatively, if the previously considered highest distinguished frequency is a harmonic of $f^l$, the coherent fluctuations associated with the former can be skipped from the equation as they had been shown to fulfill $\partial \langle \tilde{u}_i^l \rangle^l / \partial x_i = 0$ in the previous step. By continuing this inductive reasoning until the lowest considered coherent frequency, one can prove that $\partial \langle \tilde{u}_i^l \rangle^l / \partial x_i = 0$ holds for all of the distinguished coherent frequencies. Further, after (3) is substituted for $\tilde{u}_i^l$, the factor $\Phi_i^l e^{\sqrt{-1}\phi_0} + \underline{\Phi}_i^l e^{-\sqrt{-1}\phi_0}$ can be excluded from the phase average, as it is constant for the fixed phase value $\phi_0$. Therefore, as follows from (7c), only the modulation signal $A^l$ is actually phase averaged and the resultant value is surely nonzero:

$$\frac{\partial \langle \tilde{u}_i^l \rangle^l}{\partial x_i} = \langle A^l \rangle^l \frac{\partial}{\partial x_i} \left( \Phi_i^l e^{\sqrt{-1}\phi_0} + \underline{\Phi}_i^l e^{-\sqrt{-1}\phi_0} \right) = 0. \tag{7c}$$

This, on the other hand, implies that the expression in brackets (i.e., the excluded factor) needs to be zero to equal the right-hand side. Since exactly the same factor appears in $\partial \tilde{u}_i^l / \partial x_i$ once (3) is substituted for $\tilde{u}_i^l$, it can be stated that all coherent fluctuations fulfill the incompressible continuity equation, as do the stochastic ones (as a residual of the total fluctuations) as expressed in Eqs. (7d):

$$\frac{\partial \bar{u}_i}{\partial x_i} = 0, \quad \frac{\partial \tilde{u}_i^l}{\partial x_i} = 0, \quad \frac{\partial u_i''}{\partial x_i} = 0. \tag{7d}$$

In order to derive the kinetic energy budget equations, Ref. [8] proposed multiplying the momentum equations governing particular velocity field components by their respective fluctuations and then phase averaging them before time averaging them in the final step. Unfortunately, it is not feasible to express momentum equations of the coherent fluctuations defined as in (3). Nevertheless, energy budget equations are still accessible. They can be derived by considering the product of the momentum equation of total velocity with particular fluctuations and further by taking their temporal averages (phase averaging can be omitted since $\overline{\langle a \rangle^l} = \bar{a}$). After a few transformations and regrouping the terms in a convenient manner, the result can be written in its nondimensional form as follows (note that the Reynolds number Re which appears here depends on the specific scales used

for nondimensionalization):

$$\overline{\bar{u}_i\left[\frac{\partial}{\partial\tau}+\left(\bar{u}_j+\sum_m\tilde{u}_j^m+u_j''\right)\frac{\partial}{\partial x_j}\right]\left(\bar{u}_i+\sum_m\tilde{u}_i^m+u_i''\right)}$$
$$=\overline{\bar{u}_i\left[-\frac{\partial}{\partial x_i}\left(\bar{p}+\sum_m\tilde{p}^m+p''\right)+\mathrm{Re}^{-1}\nabla^2\left(\bar{u}_i+\sum_m\tilde{u}_i^m+u_i''\right)\right]}, \tag{8a}$$

$$\bar{\mathcal{L}}+\bar{\mathcal{C}}=-\sum_m\tilde{\mathcal{P}}^m-\mathcal{P}''-\bar{\epsilon}+\bar{\mathcal{D}}, \tag{8b}$$

$$\overline{\tilde{u}_i^l\left[\frac{\partial}{\partial\tau}+\left(\bar{u}_j+\sum_m\tilde{u}_j^m+u_j''\right)\frac{\partial}{\partial x_j}\right]\left(\bar{u}_i+\sum_m\tilde{u}_i^m+u_i''\right)}$$
$$=\overline{\tilde{u}_i^l\left[-\frac{\partial}{\partial x_i}\left(\bar{p}+\sum_m\tilde{p}^m+p''\right)+\mathrm{Re}^{-1}\nabla^2\left(\bar{u}_i+\sum_m\tilde{u}_i^m+u_i''\right)\right]}, \tag{9a}$$

$$\tilde{\mathcal{L}}^l+\tilde{\mathcal{C}}^l=\tilde{\mathcal{P}}^l-\hat{\mathcal{P}}^l+\tilde{\mathcal{T}}_+^l-\tilde{\mathcal{T}}_-^l-\tilde{\epsilon}^l+\tilde{\mathcal{D}}^l, \tag{9b}$$

$$\overline{u_i''\left[\frac{\partial}{\partial\tau}+\left(\bar{u}_j+\sum_m\tilde{u}_j^m+u_j''\right)\frac{\partial}{\partial x_j}\right]\left(\bar{u}_i+\sum_m\tilde{u}_i^m+u_i''\right)}$$
$$=\overline{u_i''\left[-\frac{\partial}{\partial x_i}\left(\bar{p}+\sum_m\tilde{p}^m+p''\right)+\mathrm{Re}^{-1}\nabla^2\left(\bar{u}_i+\sum_m\tilde{u}_i^m+u_i''\right)\right]}, \tag{10a}$$

$$\mathcal{L}''+\mathcal{C}''=\sum_m\hat{\mathcal{P}}^m+\mathcal{P}''-\epsilon''+\mathcal{D}'', \tag{10b}$$

where the particular terms are defined as

$$\bar{\mathcal{L}}=\frac{\partial\bar{k}}{\partial\tau},\quad \tilde{\mathcal{L}}^l=\frac{\partial\tilde{k}^l}{\partial\tau},\quad \mathcal{L}''=\frac{\partial k''}{\partial\tau},\quad \bar{\mathcal{C}}=\bar{u}_j\frac{\partial\bar{k}}{\partial x_j},\quad \tilde{\mathcal{C}}^l=\bar{u}_j\frac{\partial\tilde{k}^l}{\partial x_j},\quad \mathcal{C}''=\bar{u}_j\frac{\partial k''}{\partial x_j},$$

$$\tilde{\mathcal{P}}^l=-\overline{\tilde{u}_i^n\tilde{u}_j^l}\frac{\partial\bar{u}_i}{\partial x_j},\quad \hat{\mathcal{P}}^l=-\overline{u_i''u_j''\frac{\partial\tilde{u}_i^l}{\partial x_j}},\quad \mathcal{P}''=-\overline{u_i''u_j''}\frac{\partial\bar{u}_i}{\partial x_j},$$

$$\tilde{\mathcal{T}}_+^l=-\frac{1}{2}\sum_{m,n}\overline{\tilde{u}_i^l\tilde{u}_j^m\frac{\partial\tilde{u}_i^n}{\partial x_j}},\quad \tilde{\mathcal{T}}_-^l=-\frac{1}{2}\sum_{m,n}\overline{\tilde{u}_i^n\tilde{u}_j^m\frac{\partial\tilde{u}_i^l}{\partial x_j}},$$

$$\bar{\epsilon}=2\mathrm{Re}^{-1}\bar{s}_{ij}\bar{s}_{ij},\quad \tilde{\epsilon}^l=2\mathrm{Re}^{-1}\overline{\tilde{s}_{ij}^l\tilde{s}_{ij}^l},\quad \epsilon''=2\mathrm{Re}^{-1}\overline{s_{ij}''s_{ij}''},$$

$$\bar{\mathcal{D}}=\frac{\partial}{\partial x_j}\left(-\bar{p}\bar{u}_j-\sum_m\overline{\tilde{u}_i^m\tilde{u}_j^m}\bar{u}_i-\overline{u_i''u_j''}\bar{u}_i+2\mathrm{Re}^{-1}\bar{s}_{ij}\bar{u}_i\right),$$

$$\tilde{\mathcal{D}}^l=\frac{\partial}{\partial x_j}\left(-\overline{\tilde{p}^l\tilde{u}_j^l}-\frac{1}{2}\overline{\tilde{u}_i^n\tilde{u}_j^m\tilde{u}_i^l}-\overline{u_i''u_j''\tilde{u}_i^l}+2\mathrm{Re}^{-1}\overline{\tilde{s}_{ij}^l\tilde{u}_i^l}\right),$$

$$\mathcal{D}''=\frac{\partial}{\partial x_j}\left(-\overline{p''u_j''}-\frac{1}{2}\sum_m\overline{(\tilde{u}_j^m+u_j'')u_i''u_i''}+2\mathrm{Re}^{-1}\overline{s_{ij}''u_i''}\right),$$

$$\bar{s}_{ij}=\frac{1}{2}\left(\frac{\partial\bar{u}_i}{\partial x_j}+\frac{\partial\bar{u}_j}{\partial x_i}\right),\quad \tilde{s}_{ij}^l=\frac{1}{2}\left(\frac{\partial\tilde{u}_i^l}{\partial x_j}+\frac{\partial\tilde{u}_j^l}{\partial x_i}\right),\quad s_{ij}''=\frac{1}{2}\left(\frac{\partial u_i''}{\partial x_j}+\frac{\partial u_j''}{\partial x_i}\right).$$

TABLE VII. Terms of the stochastic energy budget (10a) (based on experiment 3).

| $x/H$ | 0.22 | 0.23 | 0.23 | 0.36 |
|---|---|---|---|---|
| $y/H$ | −0.34 | −0.26 | −0.35 | −0.37 |
| $-\mathcal{C}''$ | $3.32 \pm 0.38$ | $5.09 \pm 0.62$ | $1.14 \pm 0.20$ | $0.32 \pm 0.09$ |
| $\sum_l \hat{\mathcal{P}}^l$ | $3.34 \pm 0.18$ | $1.47 \pm 0.08$ | $1.52 \pm 0.07$ | $0.22 \pm 0.01$ |
| $\mathcal{P}''$ | $0.43 \pm 0.07$ | $-0.65 \pm 0.13$ | $-0.06 \pm 0.04$ | $0.38 \pm 0.05$ |
| $-\epsilon''$ | $-6.67 \pm 0.12$ | $-5.79 \pm 0.11$ | $-4.64 \pm 0.04$ | $-1.48 \pm 0.02$ |
| $\mathcal{D}''$ | $-0.84 \pm 0.85$ | $-1.60 \pm 1.81$ | $1.16 \pm 0.46$ | $0.35 \pm 0.31$ |
| $\zeta$ | −0.42 | −1.47 | −0.89 | −0.21 |

The form of Eqs. (8a) to (10a) is slightly different than those of Ref. [8], as they contain some additional terms. Therefore, the interpretation of particular elements of the derived energy budget should be easily transferrable. The left-hand sides (LHS) represent rates of change of particular energy components ($\mathcal{L}$ denotes a local unsteadiness and $\mathcal{C}$ a convective component; the subscripts and superscripts are skipped for simplicity). The right-hand sides (RHS) represent the causes of these changes. They can be subdivided into three groups: energy exchange rate $\mathcal{P}$ and $\mathcal{T}$, energy dissipation rate $\epsilon$, and diffusive energy transport rate $\mathcal{D}$.

Within the first group, one can distinguish stochastic energy production by the mean flow $\mathcal{P}''$, stochastic energy production by the $l$th coherent fluctuation $\hat{\mathcal{P}}^l$, and the $l$th coherent energy production from the mean flow $\tilde{\mathcal{P}}^l$. Note that these terms redistribute energy between different energy types, appearing on the RHS of the complementary energy equations with opposite signs, accordingly. Terms $\tilde{\mathcal{T}}^l_+$ and $\tilde{\mathcal{T}}^l_-$ share this property as well; however, they appear only in particular coherent energy equations. This allows analogical interpretation of the aforementioned terms. By applying a sign convention analogous to the one used for the production terms, $\tilde{\mathcal{T}}^l_+$ can be called a source term of coherent energy of $\tilde{\mathbf{u}}^l$ while $\tilde{\mathcal{T}}^l_-$ acts as a sink. Nevertheless, these two are aggregated into a single term for the purposes of presenting the results and referred to as triadic production hereafter. The second group, i.e., mean, coherent, and stochastic dissipation terms $\bar{\epsilon}$, $\tilde{\epsilon}^l$, $\epsilon''$, remove energy from the system at their respective levels by dissipating it into heat. In each case, they appear on the RHS of the corresponding energy equation with a negative sign. Finally, the last group redistributes different energy types in a spatial sense (there is no exchange between different types of energy due to diffusive terms). They vanish after integration across entire flow domain (based on the divergence theorem).

### B. Energy budget

All terms of the energy budgets, Eqs. (8a) to (10a), were evaluated using the data gathered in experiments 2 and 3 (the stochastic part was only evaluated based on experiment 3, since the spatial resolution of experiment 2 is not sufficient). Note that it has been assumed that all out-of-plane gradients of the mean velocity field vanish due to the flow's symmetry (measurements are taken at the flume's midplane) as well as out-of-plane gradients of the coherent velocity fluctuations (this can be supported by a recent study of Ref. [47] who performed direct numerical simulation of a flow past a rectangular prism at comparable Reynolds number).

In the case of experiment 2, the contribution of components containing out-of-plane velocity (these cannot be evaluated as the experiment provides only planar data) were assumed to be proportional to the remaining, in-plane velocity based, components. Proportionality factors for the individual energy budgets' terms were approximated using the data of experiment 3 (the contribution of out-of-plane velocity appears to be of the order of 10%). Diffusion terms were evaluated without acknowledging their pressure components as the latter were not accessible. Thus the pressure does contribute substantially to the residuals $\zeta$. The results are displayed in the following figures and in Table VII.

Note that the square root of the averaged turbulent kinetic energy $\sqrt{k_x'}$ [see (1)] was used as the normalization velocity scale, $H/U_\infty$ (the convection time scale) was used as the reference time scale, and $H$ was used as the normalization length scale. Gaussian smoothing (with the kernel's standard deviation equals roughly $0.01H$) has been applied prior to plotting. The methodology and results assessing the uncertainty level of the particular energy budgets' terms are presented in Appendix E.

The kinetic energy budgets of the mean velocity (8a) evaluated at consecutive downstream positions of experiment 2 are presented in Fig. 14. It appears that the convection term $\bar{\mathcal{C}}$ is roughly balanced by the diffusion term $\bar{\mathcal{D}}$ almost everywhere except for a few locations and that the remaining terms are mostly negligible. A considerable amount of energy is drained from the mean flow (in the initial station) at the locations of the small and medium wakes, which is then transferred to coherent motions through the production term $\sum_l \tilde{\mathcal{P}}^l$. At the same time, $\mathcal{P}''$ transfers energy to the stochastic part; however, this flux, at its peak, accounts for only roughly 30% of $\sum_l \tilde{\mathcal{P}}^l$. Excitation of the stochastic motions is strongest at the edges of the wakes, which is opposite to the coherent motions' production that peaks at the centers of the wakes. At the second downstream position, one can observe a relatively strong stochastic production term at $y/H \simeq -0.13$, which is associated with the shear layer separated from the big bar [see Fig. 5(b)]. Formation of the shedding of the biggest bar can be spotted at the farthest station, where the coherent production term appears active in the big wake's area. However, as might be inferred from, e.g., Fig. 11(a), the formation of the big wake starts just around this downstream position and thus the energy transfer is not as prominent as in the cases of the other two wakes at the first station. Note that the results derived from experiment 3 are in good agreement. Values of the residuals are rather large but it only exceeds the cumulative uncertainty of the remaining terms (see Table X) at the closest downstream position, where the pressure's contribution might be particularly important (this can be inferred based on, e.g., large curvature of the mean streamlines; see Fig. 5).

Figure 15 shows relative contributions of the mean energy budget terms averaged across the transverse direction. At all of the stations, except for $x/H = 0.24$, convection plays the dominant role, accounting for almost the entire net gain. The major loss, on the other hand, can be attributed to the residual, which reflects the pressure and the contribution of the out-of-plane motion. It is worth noting that the residual's uncertainty drops significantly after averaging across the $y$ direction (note the error bars). In the case of $x/H = 0.24$, the situation is reversed; the convection term acts as a sink whereas the residual provides most of the energy. Interestingly, the relative mean energy balance seems to be almost identical at stations $x/H = 0.07$ and $x/H = 0.57$. This can be linked to the fact that both are evaluated in the vicinity of the fluctuations intensity peaks of particular wakes. A similar energy balance is also reported by Ref. [15], who considered a flow past a wall-mounted pyramid, focusing at the area around the shedding intensity peak. The authors show that the entire gain of the mean energy is due to the convection term, whereas the loss splits between the production term and the pressure term in the proportion of 30% and 70%.

Figures 16 and 17 present kinetic energy budgets (9a) of the primary coherent motions, i.e., sheddings. Coherent motions of the two smaller wakes originate close to the bars, where a large energy flux is injected into each of these motions through the production terms $\tilde{\mathcal{P}}^{\mathrm{II}}$ and $\tilde{\mathcal{P}}^{\mathrm{III}}$ as shown in Fig. 16(a) [these correspond to peaks in the energy budget of the mean velocity; see Fig. 14(a)]. The energy balances of both sheddings look very similar to one another. The convection term $\tilde{\mathcal{C}}^l$ is positive (though small) at the center, which means that the energy is already decaying there (i.e., it is decreasing as it advances downstream). It is mainly drained by the diffusion term $\tilde{\mathcal{D}}^l$, which transfers it in the transverse direction ($\tilde{\mathcal{D}}^l$ is positive while $\tilde{\mathcal{C}}^l$ is negative at the wakes' edges), causing the sheddings' transverse growth. At the same time, part of the energy is lost to the stochastic fluctuations through the production term $\hat{\mathcal{P}}^l$. In both cases, there is a considerable imbalance at the center, largely exceeding the cumulative uncertainty of the other budgets' terms. This might be caused by high-pressure gradients which are not resolved here but are likely to appear closely behind the bars, in recirculation areas.

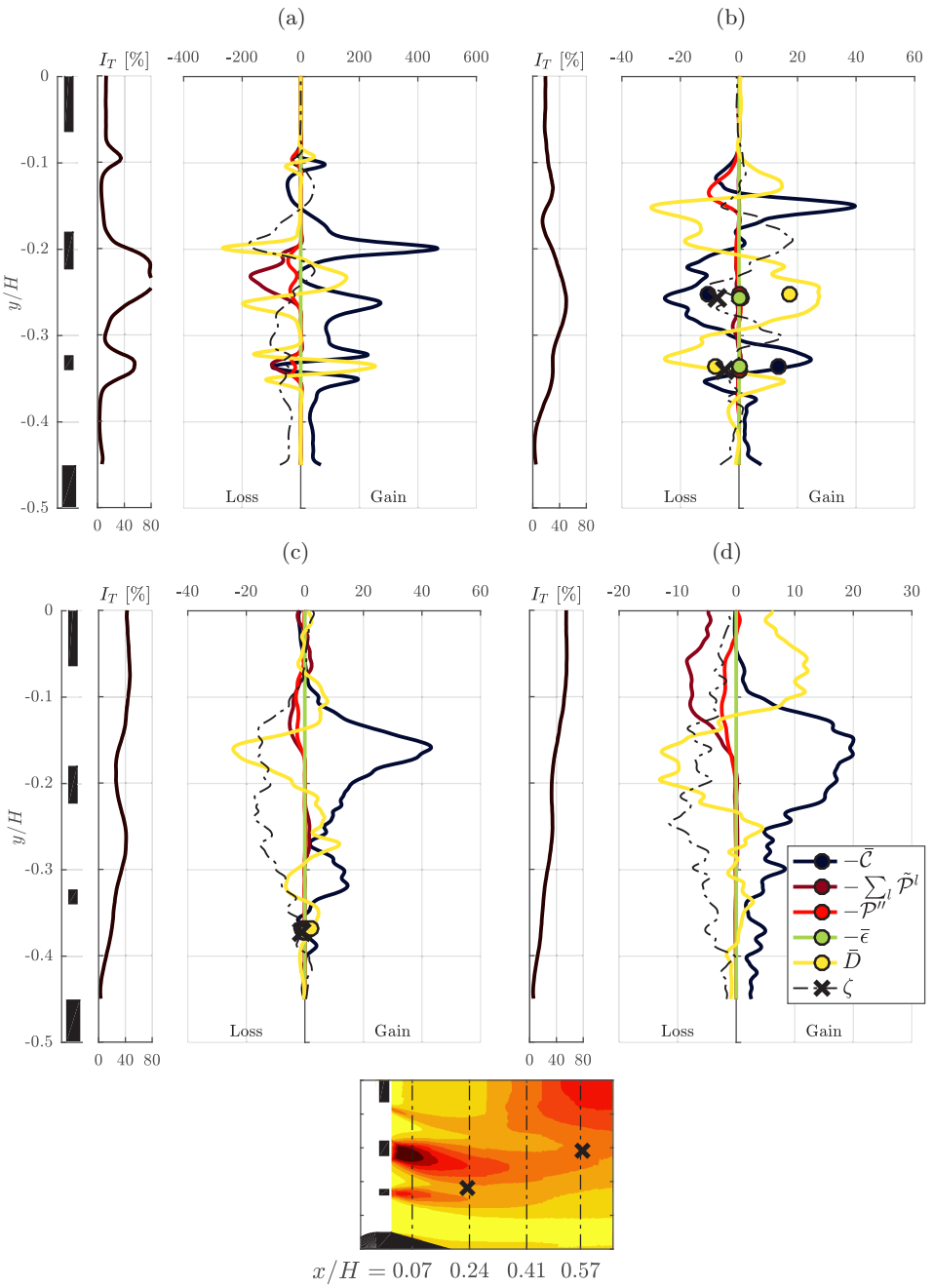


FIG. 14. Terms of the mean energy budget (8a) and the affiliated fluctuation intensity profiles at $x/H =$ (a) 0.07, (b) 0.24, (c) 0.41, and (d) 0.57 (lines are based on experiment 2 and markers are based on experiment 3). A reproduction of Fig. 5(b) is attached at the very bottom.

It should be noted that these budgets resemble the turbulent kinetic energy balance of a self-similar wake, as reported in, e.g., Refs. [48,49]. Both convection and diffusive terms behave qualitatively in the same manner. The production term $\hat{\mathcal{P}}^l$, which can be seen as an energy sink from the perspective of a coherent motion, follows a trend similar to that of the dissipation term of the self-similar

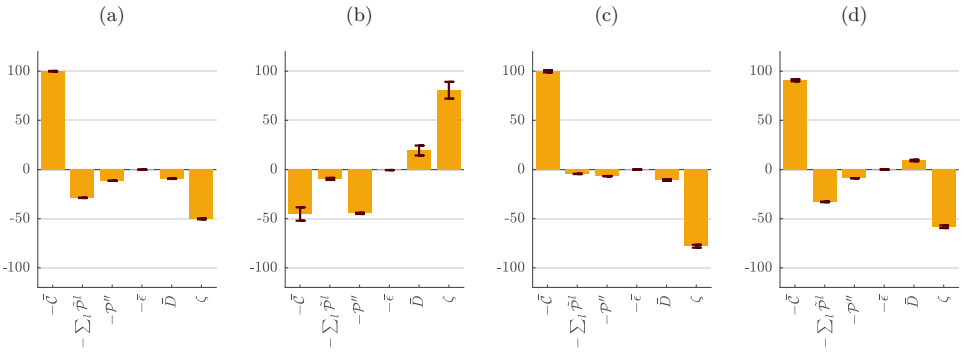


FIG. 15. Terms of the mean energy budget (8a) averaged across the transverse direction at $x/H =$ (a) 0.07, (b) 0.24, (c) 0.41, and (d) 0.57 (values are expressed as percentages of the respective total gains, based on experiment 2).

wake's budget. A clear difference appears in the context of the production term $\tilde{\mathcal{P}}^l$, the main energy source. In the case of the budget considered in this work, it reaches its maximum at the wake's center, whereas in the case of a developed self-similar wake the production term is roughly zero at the center line and peaks at the wake's edges. This has to do with the fact that in a developed planar wake $u'_{1\mathrm{rms}} \simeq u'_{2\mathrm{rms}}$ at the center line, whereas in the near wake where shedding is effective $\tilde{u}^l_{1\mathrm{rms}} \ll \tilde{u}^l_{2\mathrm{rms}}$. It is also worth mentioning that turbulent pressure diffusion, measured in Ref. [49], accounted for up to 20% of the respective convection term, which was the major term of their budget.

Similarity between the two smaller wakes is preserved at the second downstream position as illustrated in Fig. 16(b). Both sheddings are driven by convection at their centers while production by the mean flow is negligible (although one should bear in mind the considerable uncertainty of the production terms at this station; see Table X). Both sheddings continue to expand in the transverse direction through the diffusion term. The stochastic fluctuation production $\hat{\mathcal{P}}^l$ appears as a major energy sink to both wakes. Additionally, in the case of the smaller wake, considerable energy is removed by the triadic production term $\mathcal{T}^l_+ - \mathcal{T}^l_-$. Good agreement between the results of experiments 2 and 3 should also be noted. The residual levels, although still large, are now smaller than the sums of the uncertainties of all the terms, which suggests that the pressure term is not of primary importance any longer.

Figure 17 presents the kinetic energy budget at two consecutive downstream positions where the primary coherent motions $\tilde{\mathbf{u}}^{\mathrm{I}}$ and $\tilde{\mathbf{u}}^{\mathrm{II}}$ are relatively energetic. The budget of the medium bar's shedding $\tilde{\mathbf{u}}^{\mathrm{II}}$ seems to be changed only slightly, and its qualitative shape is preserved. Two characteristic features should be highlighted though. Energy is drained by the production term $\tilde{\mathcal{P}}^l$ (the loss firmly exceeds the uncertainty of the production term). This is a result of $\partial\bar{u}_2/\partial x_2$ turning positive at these downstream locations, which is enforced by the large, low-pressure recirculation area behind the big bar curving the mean flow toward the center line (see Fig. 5). The other particular feature appears at $x/H = 0.57$, where an additional drain, i.e., $\mathcal{T}^l_+ - \mathcal{T}^l_-$, appears in the budget of $\tilde{\mathbf{u}}^{\mathrm{II}}$. Its value is of the order of the stochastic fluctuations production $\hat{\mathcal{P}}^l$, which is the main sink of the budget. This is very similar to what is observed in the context of the smallest shedding at $x/H = 0.24$ (see Fig. 16(b)].

The budgets associated with the big shedding are not very conclusive (yet they are plotted for completeness). The two dominant factors are convection $\tilde{\mathcal{C}}^l$ and production $\tilde{\mathcal{P}}^l$, which drives the motion (especially at $x/H = 0.57$). Diffusion is also relatively large; however, the associated uncertainty makes it impossible to see any clear trend. The last nonzero term that appears in the budget is the production of stochastic fluctuations, which, however, stays at a small level. This picture is not similar to what is observed in the initiation of the other two sheddings. It should be noted though that, unlike in the other two cases, this is still a production area of the large shedding [i.e., the energy grows with downstream position; see Fig. 11(a)].

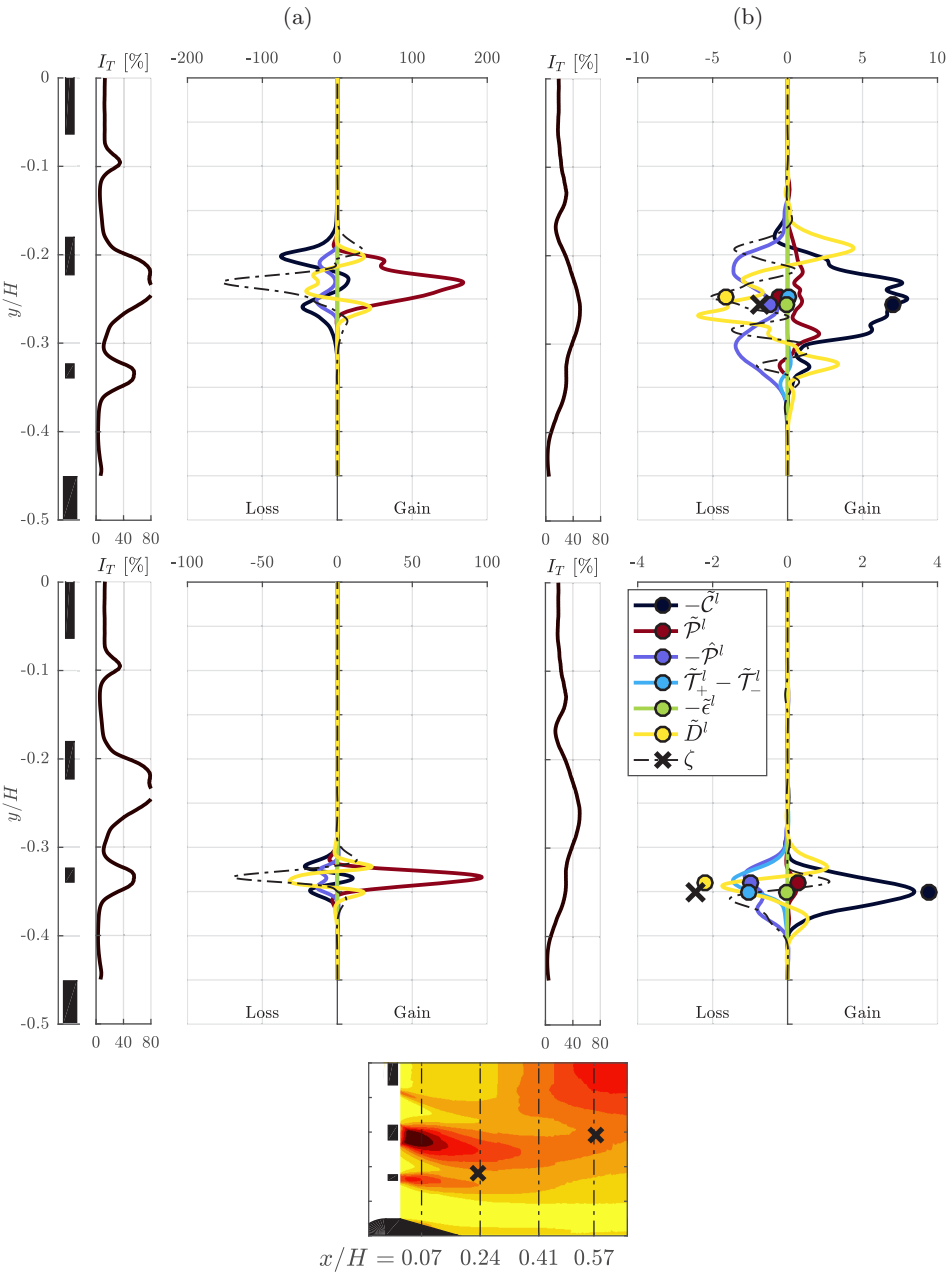


FIG. 16. Terms of the coherent energy budget (9a) evaluated for the primary coherent fluctuations ($\tilde{\mathbf{u}}^{\mathrm{II}}$, upper plots; $\tilde{\mathbf{u}}^{\mathrm{III}}$, lower plots) and the affiliated fluctuations intensity profiles at $x/H =$ (a) 0.07 and (b) 0.24 (lines are based on experiment 2 and markers are based on experiment 3). A reproduction of Fig. 5(b) is attached at the very bottom.

Figure 18 presents relative contributions of the coherent energy budget terms associated with the primary coherent motions averaged across the transverse direction. Further similarities between behaviors of the particular wakes emerge. In particular, Figs. 18(b), 18(c), and 18(g) show the relative coherent budget terms in the vicinity of the respective shedding maxima. In each case, the

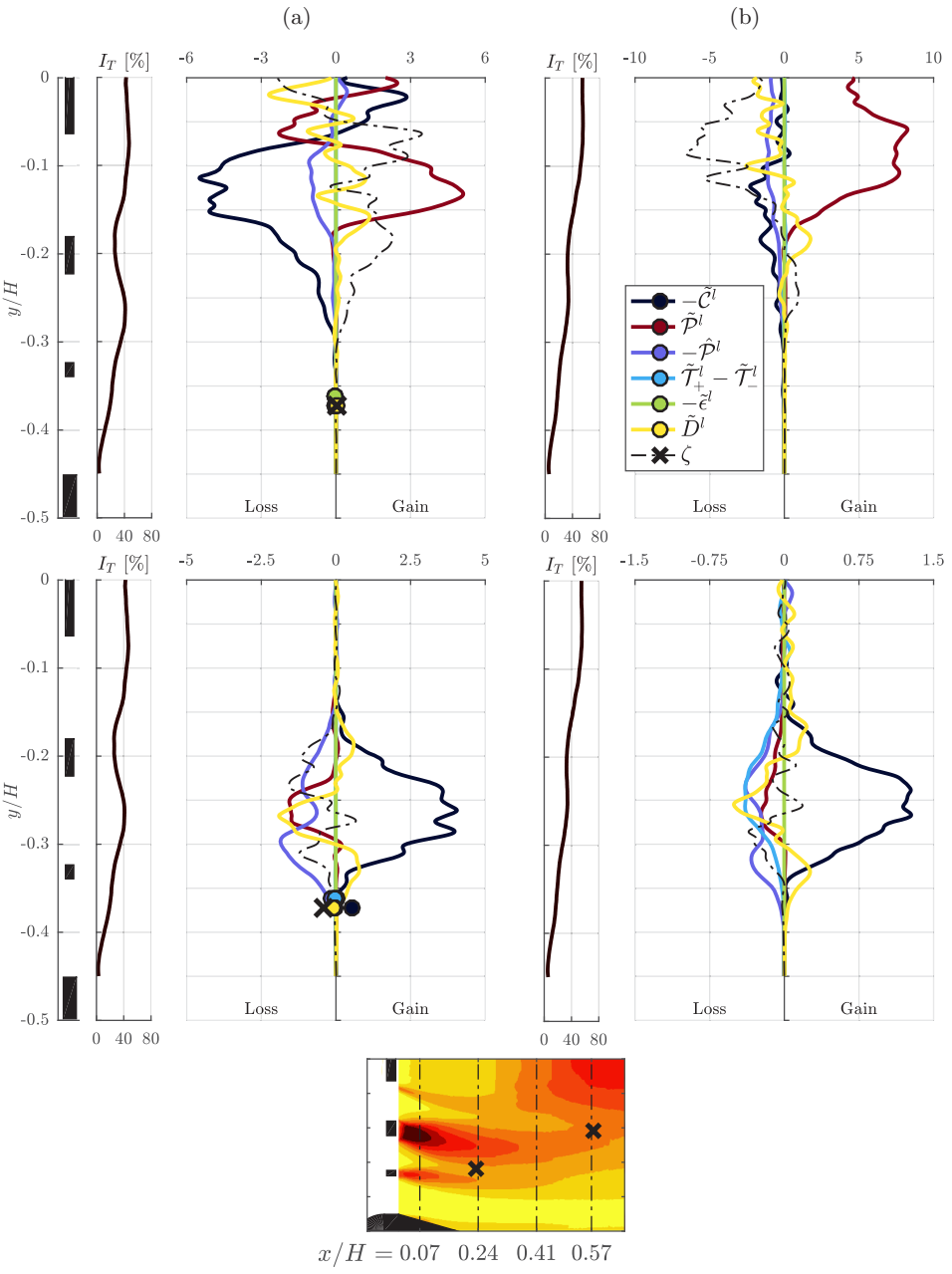


FIG. 17. Terms of the coherent energy budget (9a) evaluated for the primary coherent fluctuations ($\tilde{\mathbf{u}}^{\mathrm{I}}$, upper plots; $\tilde{\mathbf{u}}^{\mathrm{II}}$, lower plots) and the affiliated fluctuation intensity profiles at $x/H =$ (a) 0.41 and (b) 0.57 (lines are based on experiment 2 and markers are based on experiment 3). A reproduction of Fig. 5(b) is attached at the very bottom.

budget is driven almost exclusively by the production term $\tilde{\mathcal{P}}^l$. This is balanced by the convection, the stochastic fluctuations production, and the residual terms. The latter account for the majority of losses, i.e., 40–60%, and the former two account for further 20–40. Reference [15] reported a similar tendency in the flow past a pyramid. The energy balance of its first shedding harmonic was

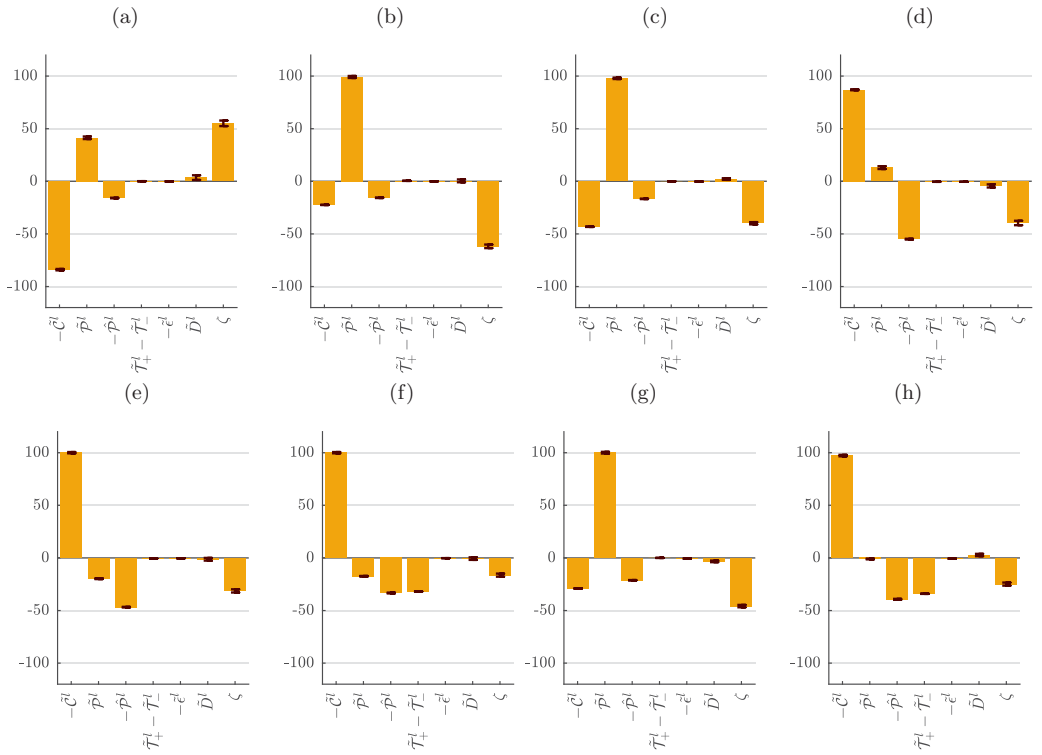


FIG. 18. Terms of the coherent energy budget (9a) averaged across the transverse direction evaluated for $\tilde{\mathbf{u}}^{\mathrm{I}}$ at $x/H =$ (a) 0.41 and (b) 0.57; for $\tilde{\mathbf{u}}^{\mathrm{II}}$ at $x/H =$ (c) 0.07, (d) 0.24, (e) 0.41, and (f) 0.57; and for $\tilde{\mathbf{u}}^{\mathrm{III}}$ at $x/H =$ (g) 0.07 and (h) 0.24 (values are expressed as percentages of the respective total gains, based on experiment 2).

driven entirely by the production term, while losses were caused by the convection term (20%) and the stochastic fluctuations production (70%, referred to as residual in Ref. [15]). The pressure work contribution is mentioned to be minor. On the other hand, Figs. 18(f) and 18(h) also bear significant resemblance, showing the relative coherent energy budget in the areas of the respective wakes' intersection points. The budgets are convection driven, spreading the energy among the triadic production, the stochastic fluctuations production, and the residual term by a roughly equal amount. Additionally in the case of the medium wake, as already mentioned above, 15% of the coherent energy losses are transferred back to the mean flow through the production term [see Figs. 18(e) and 18(f)].

The budgets of the secondary coherent motions are displayed in Fig. 19. It seems that pairs $\tilde{\mathbf{u}}^{\mathrm{II-I}}$ and $\tilde{\mathbf{u}}^{\mathrm{II+I}}$ and $\tilde{\mathbf{u}}^{\mathrm{III-II}}$ and $\tilde{\mathbf{u}}^{\mathrm{III+II}}$, despite the high noise level of the former, behave in a similar qualitative manner, which confirms that they are governed by the same physics. All of the secondary motions are primarily driven by the triadic production term $\tilde{\mathcal{T}}^l_+ - \tilde{\mathcal{T}}^l_-$. This energy supply comes from the primary coherent fluctuations where the triadic production term acts as an energy sink [see Figs. 16(b) and 17(b)]. Production by the mean flow, at least at the monitored streamwise stations, is either negligible ($\tilde{\mathbf{u}}^{\mathrm{III-II}}$ and $\tilde{\mathbf{u}}^{\mathrm{III+II}}$) or even slightly negative ($\tilde{\mathbf{u}}^{\mathrm{II-I}}$ and $\tilde{\mathbf{u}}^{\mathrm{II+I}}$). The latter case can be explained in a fashion similar to that of the primary shedding motion $\tilde{\mathbf{u}}^{\mathrm{II}}$ (i.e., the recirculation behind the large bar enforces positive $\partial\bar{u}_2/\partial x_2$ which leads to a negative production $\tilde{\mathcal{P}}^l$). The largest energy drainage comes through the production of stochastic fluctuations (although in the case of $\tilde{\mathbf{u}}^{\mathrm{III-II}}$ the uncertainty is too large to confidently assess this term). In the case of the higher frequency secondary motions, $\tilde{\mathbf{u}}^{\mathrm{II+I}}$ and $\tilde{\mathbf{u}}^{\mathrm{III+II}}$, convection also appears as an important source term, which suggests a spatial decay of these motions. Contrastingly, in the cases of the lower frequency secondary motion

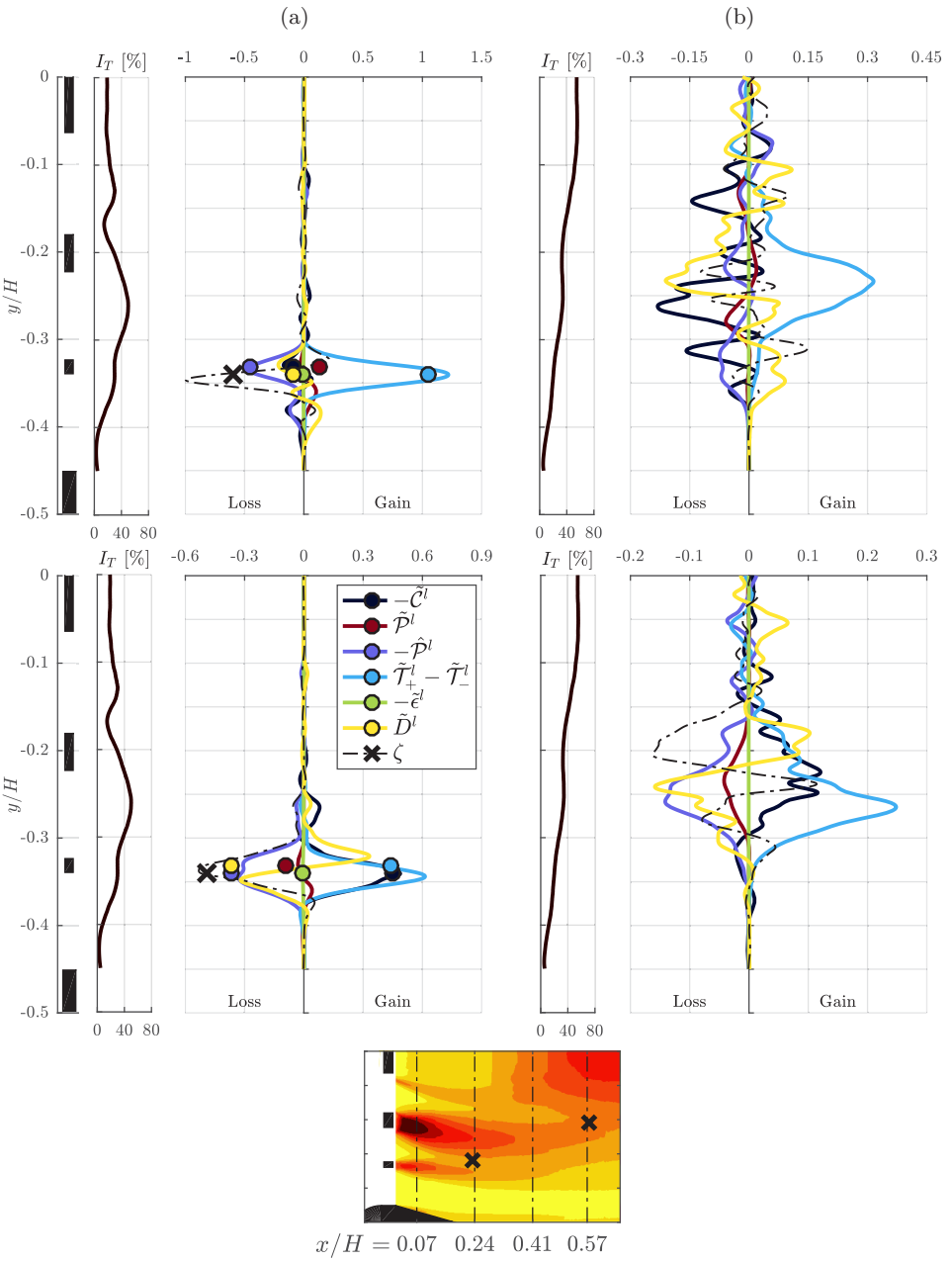


FIG. 19. Terms of the coherent energy budget (9a) evaluated for the secondary coherent fluctuations and the affiliated fluctuations intensity profiles at (a) $x/H = 0.24$ ($\tilde{\mathbf{u}}^{\mathrm{III}-\mathrm{II}}$, the upper plot; $\tilde{\mathbf{u}}^{\mathrm{III}+\mathrm{II}}$, the lower plot) and (b) $x/H = 0.57$ ($\tilde{\mathbf{u}}^{\mathrm{II}-\mathrm{I}}$, the upper plot; $\tilde{\mathbf{u}}^{\mathrm{II}+\mathrm{I}}$, the lower plot, lines are based on experiment 2 and markers are based on experiment 3). A reproduction of Fig. 5(b) is attached at the very bottom.

$\tilde{\mathbf{u}}^{\mathrm{II}-\mathrm{I}}$ and $\tilde{\mathbf{u}}^{\mathrm{III}-\mathrm{II}}$, the convection terms are rather negative. Note that the energies of $\tilde{\mathbf{u}}^{\mathrm{III}+\mathrm{II}}$ and $\tilde{\mathbf{u}}^{\mathrm{III}-\mathrm{II}}$ peak at $x/H$ equal 0.22 and 0.36 respectively, while Fig. 19(a) refers to $x/H = 0.24$, which is consistent with the observed values of convection terms. This is also in line with the observed greater persistence of $\tilde{\mathbf{u}}^{\mathrm{III}-\mathrm{II}}$ compared to $\tilde{\mathbf{u}}^{\mathrm{III}+\mathrm{II}}$, as mentioned in Sec. III. The appearance of the

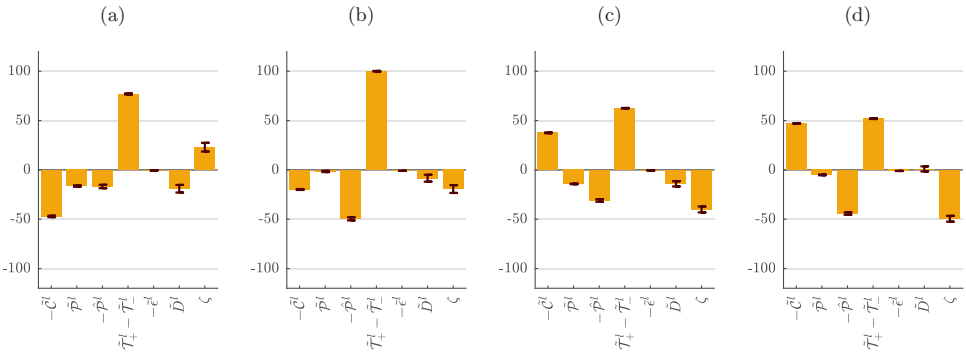


FIG. 20. Terms of the coherent energy budget (9a) averaged across the transverse direction evaluated at (a) $x/H = 0.24$ for $\tilde{\mathbf{u}}^{\mathrm{II-I}}$, (b) $x/H = 0.57$ for $\tilde{\mathbf{u}}^{\mathrm{III-II}}$, (c) $x/H = 0.24$ for $\tilde{\mathbf{u}}^{\mathrm{II+I}}$, and (d) $x/H = 0.57$ for $\tilde{\mathbf{u}}^{\mathrm{III+II}}$ (values are expressed as percentages of the respective total gains, based on experiment 2).

diffusion term seems to be similar in the budgets of $\tilde{\mathbf{u}}^{\mathrm{II+I}}$ and $\tilde{\mathbf{u}}^{\mathrm{III+II}}$. It reaches a relatively large positive value at the inner side of its respective structure and becomes opposite in its outer side, as if it tends to shift the energy toward the gap between the interacting wakes. However, due to the high uncertainty of this term, no solid conclusions can be drawn. The imbalance of the budgets of $\tilde{\mathbf{u}}^{\mathrm{III+II}}$ and $\tilde{\mathbf{u}}^{\mathrm{III-II}}$ peak at the centers of the respective structures which, again, might be caused by the missing pressure term. Alternatively, this can be the result of some important out-of-plane components' contribution not being captured in our considered experiment. Note that the results of experiment 3 agree remarkably well with those of experiment 2 (also in terms of the residuals).

Figure 20 presents relative contributions of the coherent energy budget terms associated with the secondary coherent motions averaged across the transverse direction. The triadic interactions account for the major gain, accompanied by the significant convection contribution in the case of the higher frequency secondary coherent motions [see Figs. 20(c) and 20(d)]. Losses, on the other hand, appear mostly due to the stochastic fluctuation production and the residual term in the case of the higher frequency secondary coherent motions. The pattern of the lower frequency secondary coherent motions energy losses [see Figs. 20(a) and 20(b)] is less clear; different terms contribute at different levels.

The terms of the kinetic energy budget of the stochastic fluctuations (10a) evaluated based on the data of experiment 3 are summarized in Table VII. The uncertainties of these results are estimated in the same manner as for the mean and coherent energy budgets (i.e., with the convergence intervals). At all spots, the convection term $\mathcal{C}''$ and production by coherent motions $\sum_l \hat{\mathcal{P}}^l$ are the main driving factors. Direct production by the mean flow $\mathcal{P}''$ is much smaller [even negative at $(x/H, y/H) = (0.23, -0.26)$]. The station $x/H = 0.36$ comes as an exception as all the mentioned source terms are roughly the same. This is similar to the observation in Ref. [15], which showed an equal contribution of the production by the mean flow and the coherent fluctuations. The diffusive term $\mathcal{D}''$ reaches relatively high values but it comes with very wide convergence intervals, leaving little confidence in its exact value (note that the uncertainties of the convection terms are also quite large). It appears that virtually all the dissipation is due to the stochastic fluctuations, as the values of $\epsilon''$ are almost the same as those of $\epsilon'$ presented in Table VI. Dissipation caused by the mean and coherent velocity components is negligible everywhere except the first probed downstream position $x/H = 0.07$, where both $\bar{\epsilon}$ and $\tilde{\epsilon}^l$ are of order of 0.5, which is comparable to the values summarized in Table VII (this is caused by extreme velocity gradients which appear there). The residual $\zeta$ is negative at all positions; however, it is always smaller than the respective cumulative uncertainty.

### C. Triadic energy exchange

It has been demonstrated in the previous subsection that the secondary coherent motions are excited via triadic interactions of the primary shedding modes. Their main driving term is the triadic

production $\mathcal{T}_+^l - \mathcal{T}_-^l$. This is very different from the excitation of the primary shedding motions, which are supplied by the mean production $\tilde{\mathcal{P}}^l$. Let us track the exact exchange of energy between particular coherent motions to better understand the mechanism of generation of the secondary modes.

The triadic production term is defined as the sum of contributions from interactions of all possible triads of coherent motions, see (9a), although only a few of them are non-negligible. Each of these components represents the flux between two coherent motions. For instance, component $-\frac{1}{2}\overline{\tilde{u}_i^l \tilde{u}_j^m \partial \tilde{u}_i^n / \partial x_j}$ appears as a source term (with a positive sign) in the right-hand side of a budget equation of $\tilde{\mathbf{u}}^l$ but it also appears as a sink term (with a negative sign) in the right-hand side of a budget equation of $\tilde{\mathbf{u}}^n$. Thus this term can be understood as an energy flux from the motion $\tilde{\mathbf{u}}^n$ toward $\tilde{\mathbf{u}}^l$. It should be noted that a triad $\{\tilde{\mathbf{u}}^l, \tilde{\mathbf{u}}^m, \tilde{\mathbf{u}}^n\}$ generates a nonzero contribution to the triadic production term if an associated combination $f^l \pm f^m \pm f^n$ can be equal to zero (this assumes sufficient separation between spectral content of particular coherent motions).

There are only two triads at $x/H = 0.24$, i.e., $\{\tilde{\mathbf{u}}^{\mathrm{II}}, \tilde{\mathbf{u}}^{\mathrm{III}}, \tilde{\mathbf{u}}^{\mathrm{III-II}}\}$ and $\{\tilde{\mathbf{u}}^{\mathrm{II}}, \tilde{\mathbf{u}}^{\mathrm{III}}, \tilde{\mathbf{u}}^{\mathrm{III+II}}\}$, which generate nonzero contribution to the triadic production. Similarly at $x/H = 0.57$ it is either $\{\tilde{\mathbf{u}}^{\mathrm{I}}, \tilde{\mathbf{u}}^{\mathrm{II}}, \tilde{\mathbf{u}}^{\mathrm{II-I}}\}$ or $\{\tilde{\mathbf{u}}^{\mathrm{I}}, \tilde{\mathbf{u}}^{\mathrm{II}}, \tilde{\mathbf{u}}^{\mathrm{II+I}}\}$ that generates a nonzero contribution. The resultant fluxes are plotted in Figs. 21(a) and 21(b). Qualitative similarity between the energy transit at both stations is very clear; the corresponding curves follow the same trends. It should be noted that although lower frequency primary fluctuations $\tilde{\mathbf{u}}^{\mathrm{I}}$ and $\tilde{\mathbf{u}}^{\mathrm{II}}$ are involved in these transfers, all the exchange takes place near the higher frequency primary shedding $\tilde{\mathbf{u}}^{\mathrm{II}}$ and $\tilde{\mathbf{u}}^{\mathrm{III}}$.

Figures 21(c) and 21(d) display diagrams presenting fluxes associated with the integrals of transverse profiles of the particular triadic production components [see Figs. 21(a) and 21(b); note that the used normalization scales for turbulence intensity, time, and length scales are equal to $\sqrt{k_x'}$, $H/U_\infty$, and $H$ respectively]. It appears that the fluxes observed in the two cases are roughly proportional. The energy exchange between the primary sheddings is minimal. The higher frequency primary motion gives out roughly an equal amount of energy to both secondary motions. At the same time, the lower frequency primary motion drains the high-frequency secondary coherent fluctuations and transmits this energy to the other secondary fluctuations. Since all of these transfers happen near the smaller of the interacting wakes and the net gain of the lower frequency primary coherent motion is minimal, it can be speculated that it is actually an indication of a partition of the higher frequency primary coherent motion. The lower frequency primary coherent motions act as a catalyst only; i.e., this scenario is triggered if the influence of the lower frequency primary coherent motions is sufficient. This would explain why the appearance of the secondary coherence peaks is observed roughly near the wakes' intersection points. It is worth noting that a considerable part of the energy associated with the higher frequency primary motion is actually transmitted toward the lower frequencies, which can be seen as an inverse energy cascade.

## VI. CONCLUSIONS

The analysis of our considered multiscale flow reveals the distinctive scenario of the interaction of adjacent wakes, of nonuniform size, that happen to intersect at their early stages of development, when still dominated by sheddings. Additional quasiperiodic fluctuations are excited, in addition to the original shedding motions, whose characteristic frequencies are equal to the sum and the difference of the primary shedding frequencies (see, e.g., Fig. 8). Spatially, they become noticeable in the vicinity of the wakes' intersection point and position themselves at the shear layers of the smaller of the interacting wakes (as shown in Figs. 11 and 13. The lower frequency secondary motion appears to be particularly persistent; it lives even longer than the primary high-frequency shedding fluctuations. This spectral characteristic might be interpreted as an amplitude modulation of the smaller wake by the bigger one; however, the considerable persistence of the secondary peaks seems peculiar in this context. The appearance of this scenario is not limited to our specific case as

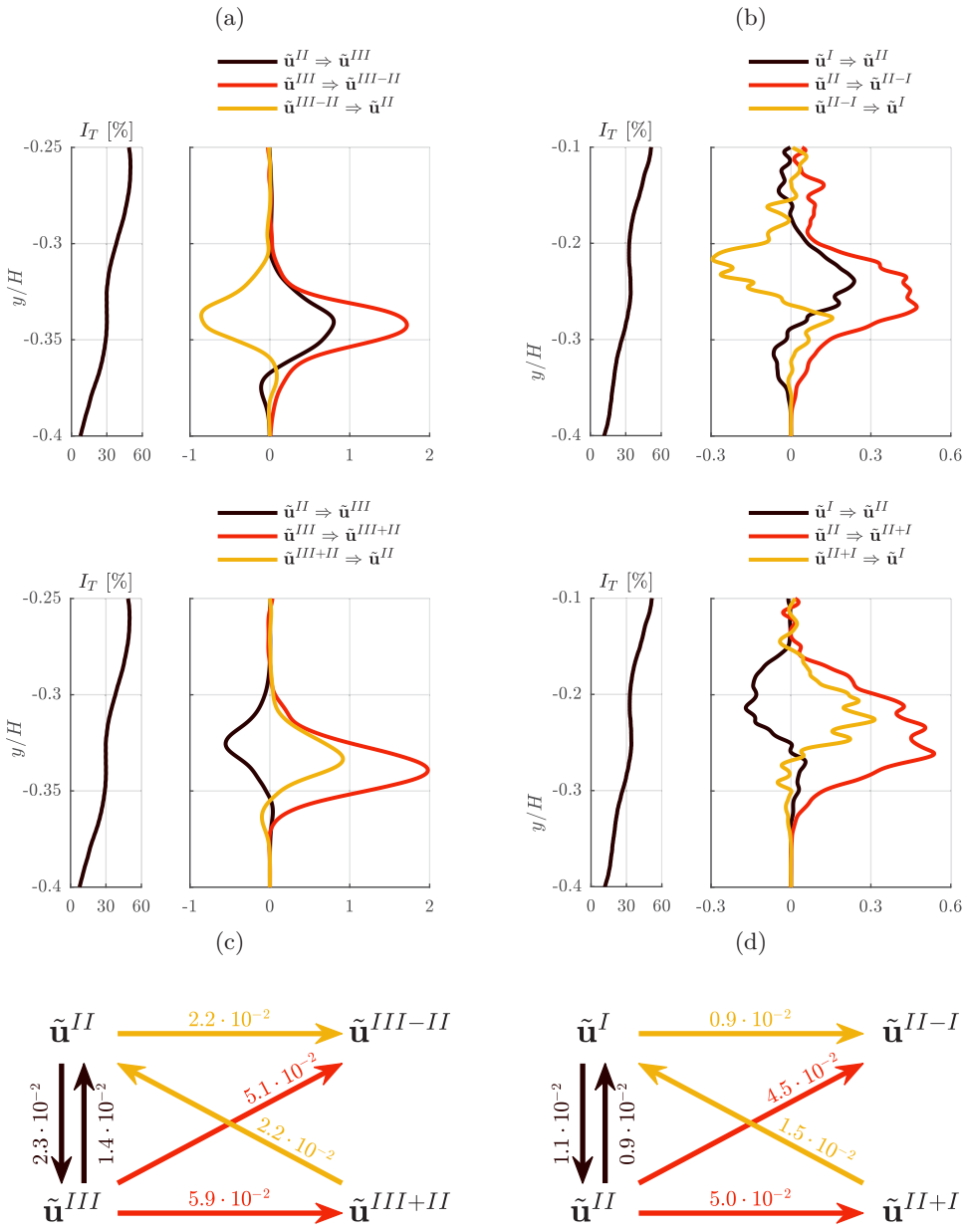


FIG. 21. Components of the triadic production term of the coherent energy budget (9a) governing energy transfer between primary and secondary coherent fluctuations and the affiliated fluctuations intensity profiles evaluated at $x/H =$ (a) 0.24 (triads $\{\tilde{\mathbf{u}}^{\mathrm{II}}, \tilde{\mathbf{u}}^{\mathrm{III}}, \tilde{\mathbf{u}}^{\mathrm{III-II}}\}$ and $\{\tilde{\mathbf{u}}^{\mathrm{II}}, \tilde{\mathbf{u}}^{\mathrm{III}}, \tilde{\mathbf{u}}^{\mathrm{III+II}}\}$) and (b) 0.57 (triads $\{\tilde{\mathbf{u}}^{\mathrm{I}}, \tilde{\mathbf{u}}^{\mathrm{II}}, \tilde{\mathbf{u}}^{\mathrm{II-I}}\}$ and $\{\tilde{\mathbf{u}}^{\mathrm{I}}, \tilde{\mathbf{u}}^{\mathrm{II}}, \tilde{\mathbf{u}}^{\mathrm{II+I}}\}$). The integrals of the transverse profiles of the particular triadic production term's components shown in diagrammatic form for $x/H =$ (c) 0.24 and (d) 0.57 (based on experiment 2).

very similar behavior had already been reported in the literature, e.g., Refs. [43–45]. On the contrary, this phenomenon might be a universal feature of multiscale flows.

An in-depth insight into the dynamics of the considered velocity fluctuations is achieved through the introduced triple decomposition of the velocity and the newly derived energy-budget equations. The extracted coherent velocity modes (see Figs. 11 and 13) clearly show that both the primary and

secondary coherent fluctuations are organized into extended zones of spatially coherent vorticity, which resembles the definition of a coherent structure proposed in Ref. [50] ("A coherent structure is a connected turbulent fluid mass with instantaneously phase-correlated vorticity over its spatial extent," p. 307). However, since the coherent fluctuations considered in the present work were not studied in the context of any structural identification methodology, classifying them as coherent structures might be too hasty. Energy maxima of the modes associated with the primary fluctuations are located closely downstream of the bars (the shedding of the biggest bar comes as an exception in this case, although likely for some other reason), whereas the maxima of the secondary coherent fluctuations are located farther downstream. This is an indication of the fact that different mechanisms are involved in the creation of these two types of coherent fluctuations. The analysis of the energy budgets provides further information about these mechanisms. The energy budgets of the primary shedding fluctuations [see Figs. 16(a) and 17(a)] show that the mean flow is their main energy source. Production by the mean flow, however, is only effective at the closest downstream position. Farther downstream, the primary fluctuations are driven by the convection term. The secondary fluctuations (see Fig. 19), on the other hand, are supplied through the triadic production term almost exclusively. This proves directly that the observed secondary coherent fluctuations are products of nonlinear triadic interactions between the primary shedding structures, which becomes particularly intense around the wakes' intersection points.

A closer look at the energy transfers between different coherent modes (see Fig. 21) shows that while the energy of the low-frequency primary mode of the interacting pair is roughly preserved, that of the high-frequency diminishes. It is split roughly equally between the two secondary modes. However, the high-frequency secondary mode further passes a considerable part of its energy to the other secondary mode, transiting it through the primary low-frequency mode. Finally, as the net effect, the low-frequency secondary motions receive most of the energy given out by the primary shedding mode. The whole scenario can be seen as a partition of the smaller of the two interacting primary sheddings into two new secondary coherent fluctuations, which is induced by the proximity of the low-frequency primary fluctuations.

It is worth noting that the transition of the energy from the high-frequency primary mode to the low-frequency secondary mode is reminiscent of the concept of an inverse energy cascade in a turbulent flow. This phenomenon was recently identified by Ref. [51] in the near wake of a fractal grid, which, similar to our considered geometry, also simultaneously forces the flow at multiple length scales. The authors show that there is an inverse energy flux along some specific directions in scale space which coexists with the forward cascade developed in other directions (the cascade is forward on average). Although the authors do not discriminate between different types of fluctuation in the aforementioned work, it can be speculated, based on our findings, that the inverse cascade appears as the result of the observed triadic interactions between the sheddings of the fractal grid's bars.

The described phenomenon exhibits potential for some flow control applications. For instance, one can imagine that an object's shedding frequency is altered through introducing another object whose wake would interact with the original wake in a desirable manner. Some further studies are needed to determine if similar behavior could be also achieved in the context of a free shear layer or a jet flow. It would also be beneficial to check which of the interacting structures' parameters, i.e., their different length or frequency scales, is crucial for the appearance of the considered phenomenon (note that in our case sheddings differed in both size and characteristic frequencies).

Another interesting observation that follows from the revised energy budgets is that the stochastic fluctuations are mainly produced from the coherent fluctuations; production by the mean flow is much weaker (see Table VII). This clearly shows that by using a multiscale geometry to trigger turbulence one can introduce energy at multiple different wave numbers at once in a well-controlled manner. Note that this was one of the motivations behind research on fractal generated turbulence in the first place (see Ref. [52]). On the other hand, it is also clearly shown in Sec. V that virtually all of the dissipation happens within the stochastic fluctuations. This could have been expected, as the length scale of the finest considered coherent fluctuations is still much larger than the dissipative scale. However, this does not need to be the case in general so no further conclusions can be drawn.

Last but not least, the current work provides another tool for analysis of various turbulent flows with embedded noticeable coherence, i.e., the developed energy budget equations and the associated triple decomposition. It is an extension of the approach proposed in Ref. [8], accommodating consideration of multiple coherent fluctuations fitted with their affiliated time-varying amplitudes.

## ACKNOWLEDGMENTS

The authors acknowledge support from THE EU through the FP7 People: Marie-Curie Actions (Grant Agreement No. 317269). We are also grateful to Dr. A. Wynn, Dr. D. Pearson, Prof. B. Ganapathisubramani, and Dr. P. J. Goulart for sharing the MATLAB implementation of the OMD algorithm (it was downloaded from http://control.ee.ethz.ch/index.cgi?page=publications&action= details&id=4094).

## APPENDIX A: ESTIMATION OF THE TURBULENT KINETIC ENERGY DISSIPATION RATE

The problem of measuring instantaneous velocity gradients in the context of PIV experiments has been approached by several researchers in the past. Hence, many different techniques that could mitigate the errors of insufficient resolution or noise have been proposed. The first issue was addressed by, e.g., Ref. [53], which proposed a method that provides corrections to the measured velocity gradients based on an assumed reference energy spectrum. The other problem was approached by, e.g., Ref. [54]. They showed that the error arising from noise can be reduced by comparing results obtained from a finer and a coarser measurement grid. In Ref. [55], the authors compared the two methods and their combinations within the context of dissipation calculations. They concluded that by applying both corrections, i.e., Ref. [53]'s method and then Ref. [54]'s method, it is possible to achieve results that are the least sensitive to resolution. This combined approach is applied in this work whenever the statistics of the velocity gradients are considered.

As discussed in Sec. III, the local axisymmetry concept (see Ref. [42]) is utilized in the present work. This theory allows us to reduce the velocity gradients' correlation tensor to a set of four invariants $\{B_1, B_2, B_3, B_4\}$ plus a vector $\boldsymbol{\gamma}$ specifying the axisymmetry direction, as defined by (A1):

$$\begin{aligned}\overline{\frac{\partial u_i'}{\partial x_m}\frac{\partial u_j'}{\partial x_n}} = {} & (-2B_1 + 2B_2 - 2B_3)(\delta_{in}\delta_{jm} + \delta_{im}\delta_{jn}) + [(8B_1 - 4B_2 + 6B_3)\delta_{mn} \\ & - (4B_3 - 2B_4 - 16B_1)\gamma_m\gamma_n]\delta_{ij} + [(-6B_3 + 4B_2)\delta_{mn} - 2B_4\gamma_m\gamma_n]\gamma_i\gamma_j \\ & - (4B_2 - 2B_3)[\gamma_i(\gamma_m\delta_{jn} + \gamma_n\gamma_{jm}) + \gamma_j(\gamma_m\delta_{in} + \gamma_n\gamma_{im})]. \end{aligned} \tag{A1}$$

The stereoscopic experiment 3 provides all three velocity component in a plane. As a result, 27 out of 54 independent elements of the velocity gradients correlation tensor can be evaluated explicitly (planar experiment 4 provides 10 independent elements). Since only seven scalars are required to use (A1), it is possible to establish an optimization procedure which finds these parameters so that (A1) is fulfilled for the known elements of the tensor in a least squares sense. The unknown elements could be further approximated using the established values of the invariants. The axisymmetry directions, which appear as a result of the optimization, seem to be very similar at all the probed locations, e.g., at the point $(x/H, y/H) = (0.36, -0.37)$ $\boldsymbol{\gamma} = \pm[0.07, 0.00, 0.99]$, which aligns predominantly with the spanwise direction. Figure 22 shows a comparison of a few derivatives' correlations evaluated explicitly with their counterparts calculated based on (A1), showing a decent match between the two.

## APPENDIX B: THEORETICAL BACKGROUND OF THE TRIPLE DECOMPOSITION

The employed triple decomposition method (Ref. [13] relies heavily on optimal mode decomposition, OMD; see Ref. [46] for an extensive description), which is a snapshot-based

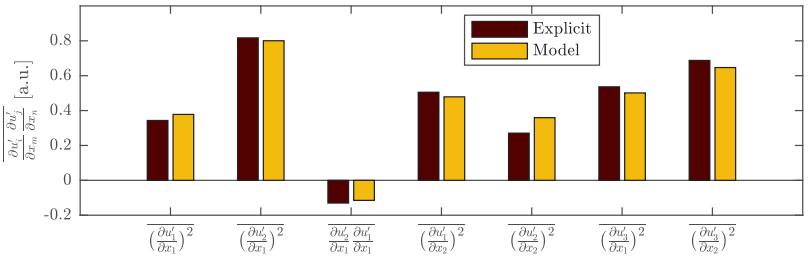


FIG. 22. Comparison of velocity gradients' correlations calculated explicitly from the data and evaluated based on the local axisymmetry model (A1) (based on experiment 3).

technique for establishing an optimal linear approximation of the system's dynamics. The underlying assumption is that two consecutive snapshots in a time-resolved sequence, $\mathbf{q}^h$ and $\mathbf{q}^{h+1}$ (the instantaneous PIV measurements), are approximately linked via linear equation (B1), where $\mathbf{D}$ is a time-invariant matrix governing the system's evolution ($m$ is the snapshot size). By elucidating the eigenvalues and eigenvectors of $\mathbf{D}$ one can get insight into the dynamics of the processes of interest; OMD is simply a method for approximating these properties:

$$\mathbf{q}^{h+1} \simeq \mathbf{D} \cdot \mathbf{q}^h, \quad \mathbf{D} \in \mathbb{R}^{m \times m}, \mathbf{q}^h \in \mathbb{R}^{m \times 1}. \tag{B1}$$

As the evolution matrix is said to be constant over the acquisition time, one can try to find an optimal $\mathbf{D}$ that would minimize the error of the approximation (B1) across all the pairs of consecutive measurements. This can be written in the form of equation (B2) ($n$ is the total number of snapshots):

$$\min_{\mathbf{D}} ||[\mathbf{q}_2, \ldots, \mathbf{q}_n] - \mathbf{D} \cdot [\mathbf{q}_1, \ldots, \mathbf{q}_{n-1}]||_2. \tag{B2}$$

The main problem that appears in a practical situation is that the number of unknowns, i.e., $m^2$, is larger than the number of constraints which makes the problem underdetermined (however, even if the system was defined, its size would make it intractable). The very essence of OMD is an idea for approximating the original $\mathbf{D}$ with a matrix $\mathbf{L} \cdot \mathbf{M} \cdot \mathbf{L}^T$ of an arbitrary rank $r$ (of course its rank needs to be lower than that of $\mathbf{D}$), which eventually leads to (B3). Here, both $\mathbf{M}$ and $\mathbf{L}$ are treated as independent optimization variables. The exact algorithm of solving this problem is described in Ref. [46]:

$$\min_{\mathbf{L},\mathbf{M}} ||[\mathbf{q}_2, \ldots, \mathbf{q}_n] - \mathbf{L} \cdot \mathbf{M} \cdot \mathbf{L}^T \cdot [\mathbf{q}_1, \ldots, \mathbf{q}_{n-1}]||_2,$$
$$\mathbf{L}^T \cdot \mathbf{L} = \mathbf{I}, \quad \mathbf{L} \in \mathbb{R}^{m \times r}, \quad \mathbf{M} \in \mathbb{R}^{r \times r}. \tag{B3}$$

After the solution of (B3) is established one can evaluate approximations of the most prominent eigenvalues and associated eigenvectors of the original evolution matrix $\mathbf{D}$, i.e., the so-called OMD eigenvalues $\xi^l_{\mathrm{OMD}}$ and OMD modes $\Phi^l_{\mathrm{OMD}}$ which are defined by (B4) and (B5) respectively ($\xi^l_{\mathbf{M}}$ and $\mathbf{z}^l$ are the eigenvalues and eigenvectors of $\mathbf{M}$, while $\Delta_\tau$ represents the temporal spacing of the snapshots):

$$\xi^l_{\mathrm{OMD}} = \frac{\ln \xi^l_{\mathbf{M}}}{\Delta_\tau}, \tag{B4}$$

$$\Phi^l_{\mathrm{OMD}} = \mathbf{L} \cdot \mathbf{z}^l. \tag{B5}$$

The adopted triple decomposition method utilizes OMD modes that can be linked to particular coherent fluctuations. They are picked based on their affiliated eigenvalues; i.e., only the modes that share their frequency with the PSD peaks and exhibit locally minimal damping (i.e., real part of the eigenvalue) are considered. An example (OMD eigenvalues evaluated in experiment 1) are presented in Fig. 23. The coincidence of the spectral peak and the OMD eigenvalues is clearly marked.

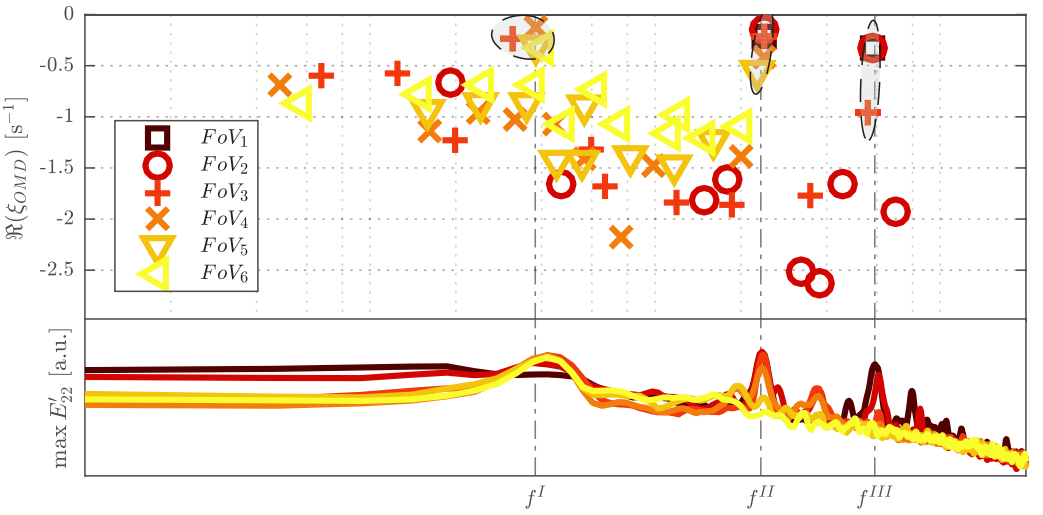


FIG. 23. OMD eigenvalues evaluated for different fields of view of experiment 1 on top of the enveloped PSD (i.e., maximum of PSD taken over the respective field of view).

## APPENDIX C: VALIDATION OF THE TRIPLE DECOMPOSITION'S RESULTS

Section IV introduces a technique of triple decomposition which is further utilized in the present work. The methodology is based on the OMD decomposition technique (see Ref. [46]) and on phase averaging. Let us briefly review the results of its application to our experimental data.

Figure 24(a) shows a representative example of the velocity signal decomposition (this velocity signal was probed near the wake of the medium bar). The total fluctuations clearly contain coherent, large-scale fluctuations, which are closely matched by the resolved coherent velocity signal. Therefore, the residual stochastic fluctuations seem to be decoupled from the underlying large-scale fluctuations. It should be noted that the amplitude of the coherent fluctuations varies in time quite

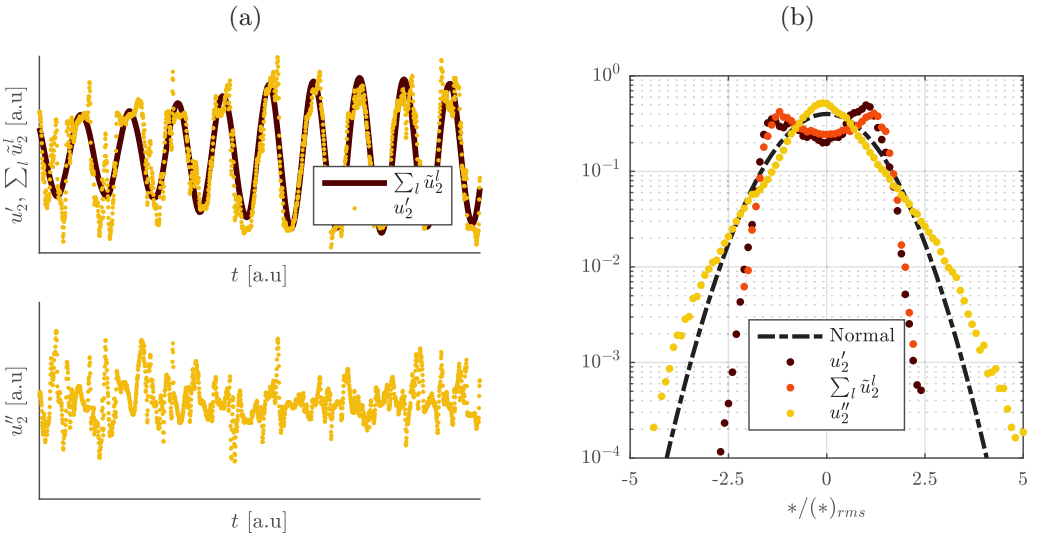


FIG. 24. Example of the triple decomposition: (a) total, coherent, and stochastic velocity fluctuations signals and (b) PDFs of the respective fluctuations' components (based on experiment 2).

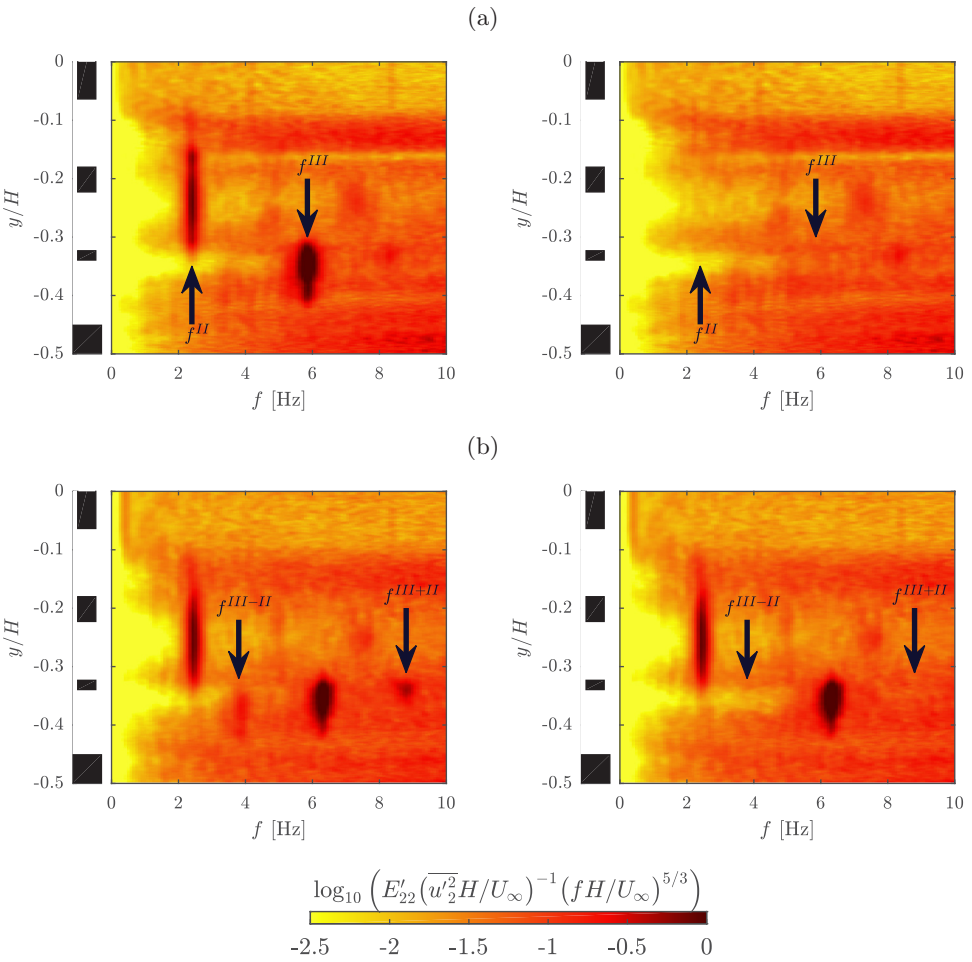


FIG. 25. PSDs of total $u_2'$ (left-hand side) and residual $u_2''$ (right-hand side) transverse velocity fluctuations after (a) OMD-based coherent fluctuations $\tilde{\mathbf{u}}^{\mathrm{II}}$ and $\tilde{\mathbf{u}}^{\mathrm{III}}$ are removed at $x/H = 0.07$, (b) phase-averaging-based coherent fluctuations $\tilde{\mathbf{u}}^{\mathrm{III-II}}$ and $\tilde{\mathbf{u}}^{\mathrm{III+II}}$ are removed at $x/H = 0.24$ (based on experiment 1).

considerably (it changes by roughly 50% within the given example). If this was not accounted for, the resultant stochastic fluctuations would still carry a prominent imprint of the coherent motion. The probability density functions (PDFs) of the velocity fluctuations presented in Fig. 24(b) are also significantly affected by the decomposition. The quasi-Gaussian PDF of the stochastic fluctuations is distinguished from the M-shaped PDF of the total fluctuations (characteristic for flows with prominent vortex shedding). This example demonstrates clearly, though qualitatively, the differences between the coherent and stochastic fluctuations as well as the efficiency of the decomposition.

A more quantitative assessment can be done by examining the PSDs of the velocity fluctuations. Figure 25 presents PSDs of the total velocity fluctuations (left-hand side) as well as PSDs of the residual velocity fluctuations (right-hand side). The arrows denote the primary shedding peaks in Fig. 25(a) ($x/H = 0.07$) and the secondary ones in Fig. 25(b) ($x/H = 0.24$). As can be seen, the left-hand side PSDs are exactly the same as the right-hand side's except for the highlighted coherence peaks, which are removed from the latter figures. A similar situation can be found at any different downstream position. This proves that the extracted coherent fluctuations, both primary and secondary, truly account for the coherent fluctuations associated with particular spectral peaks. Note that not all of energy located at the marked positions is removed from the stochastic PSDs;

TABLE VIII. Relative importance of the distinguished velocity fluctuations' components (based on experiment 2).

| | $\max_{FoV}(*)/\max_{FoV} u'_{rms}$ | | | | | | | |
|---|---|---|---|---|---|---|---|---|
| $x/H$ | $u''_{rms}$ | $\tilde{u}^{I}_{rms}$ | $\tilde{u}^{II}_{rms}$ | $\tilde{u}^{III}_{rms}$ | $\tilde{u}^{II-I}_{rms}$ | $\tilde{u}^{II+I}_{rms}$ | $\tilde{u}^{III-II}_{rms}$ | $\tilde{u}^{III+II}_{rms}$ |
| 0.07 | 0.556 | | 0.845 | 0.590 | | | | |
| 0.24 | 0.507 | | 0.851 | 0.268 | | | 0.183 | 0.132 |
| 0.41 | 0.655 | 0.802 | 0.738 | 0.050 | 0.102 | 0.100 | 0.156 | 0.115 |
| 0.58 | 0.602 | 0.835 | 0.282 | | 0.151 | 0.098 | | |
| 0.75 | 0.644 | 0.791 | 0.118 | | 0.140 | 0.064 | | |

in fact, the stochastic PSDs are quite smooth over these areas. This means that large-scale coherent fluctuations coexist with unstructured (at least in the large-scale sense) stochastic fluctuations over the same spatial and spectral domain:

The relative importance of the particular coherent fluctuations at consecutive downstream positions is summarized in Table VIII. Note that the values are normalized with the maximum root mean square of the total velocity fluctuations calculated over the respective field of view and thus the local importance can be even larger. The primary shedding fluctations account for the majority ($\sim$0.8 $\max_{FoV} u'_{rms}$) of the fluctuations at the early stages of the flow's development. The secondary fluctuations are less energetic but can still account for a significant portion of the total (almost 0.2 $\max_{FoV} u'_{rms}$). As already mentioned, there is a specific downstream position where the lower frequency secondary peak's energy exceeds the energy of the primary motions. The stochastic fluctuations account for a roughly equal share of the total fluctuations at all the downstream positions.

Figure 26 presents a comparison between the coherent fluctuations' topology resolved from different experiments; i.e., transverse profiles of the absolute values of coherent vorticity $\tilde{\omega}_3$ are plotted. Note that the results of experiments 2 and 3 correspond to $x/H = 0.24$, whereas the measurements of experiment 3 were performed at $x/H = 0.22, 0.24$. A good qualitative match between all of the measurements is observed. The peaks' positions, shapes, and widths are well preserved. Comparison shows that the difference of the vorticity peaks' values equals 13% in

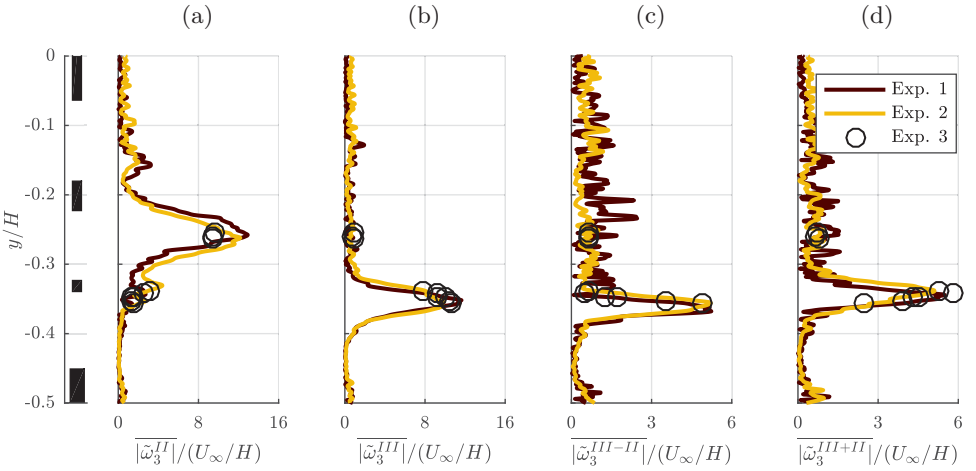


FIG. 26. Mean profiles of absolute values of coherent vorticity fluctuations, resolved from different experiments, associated to (a) $\tilde{\mathbf{u}}^{II}$ at $x/H = 0.23, 0.24$, (b) $\tilde{\mathbf{u}}^{III}$ at $x/H = 0.23, 0.24$, (c) $\tilde{\mathbf{u}}^{III-II}$ at $x/H = 0.23, 0.24$, and (d) $\tilde{\mathbf{u}}^{III+II}$ at $x/H = 0.22, 0.24$.

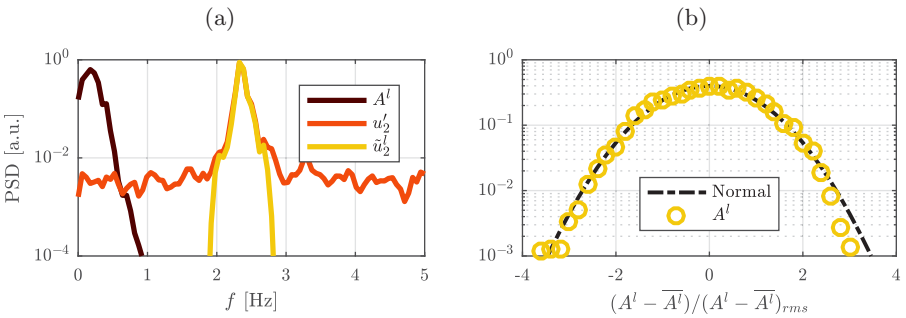


FIG. 27. (a) PSD of an amplitude signal $A^l$ on top of PSDs of associated total and coherent transverse velocity fluctuations and (b) PDF of an amplitude signal (based on experiment 2).

the worst case. Note, however, that even a slight transverse displacement of a peak can easily accommodate for this discrepancy. The good match between all of the measurements reassures us of their credibility (especially in the context of the velocity derivatives) as well as showing that the properties of the observed secondary coherent fluctuations are reproducible.

Last but not least, let us give an overview the features of the amplitude signal $A^l$. It could have already been inferred from Fig. 24(a) that the amplitude signal is mainly composed of relatively small frequencies. This is true for all of the distinguished coherent fluctuations. As a general remark, the spectral content of the amplitude signal exhibits a rapid dropoff at a frequency roughly equal to the half-width of the corresponding spectral peak of coherent velocity fluctuations. Therefore, as distance between the origin and each of the considered coherence peaks is larger than the respective half-width, coherent fluctuations are decorrelated with their amplitude signal (i.e., their spectral contents do not overlap). An example of a PSD of the amplitude signal and the affiliated coherent fluctuations is plotted in Fig. 27(a). The half-width of the coherence peak can be roughly estimated to be of the order of 0.4 Hz. The rapid cutoff of the $A^l$ spectrum starts at a comparable frequency, it drops below 0.1% of its peak value before reaching 0.8 Hz. Figure 27(b) presents a PDF of the amplitude fluctuations. It looks like it roughly follows a normal distribution, except for the right tail, which decays slightly more quickly. By surveying all measurement positions of all the experiments, it has been found that $(A^l)'_{\mathrm{rms}}/\overline{A^l}$ oscillates within bounds of 20–50%.

## APPENDIX D: VALIDATION OF THE ENERGY BUDGET'S ASSUMPTIONS

The derivation of the energy budget equations, presented in Sec. V, requires introducing a set of assumptions (6). Some of them are rather trivial (e.g., $\overline{\bar{a}} = \bar{a}$), but some may raise a concern, in particular, those governing $\langle a'' \rangle^l$, $\overline{\tilde{a}^l a''}$, or $\overline{\tilde{a}^l \tilde{a}^m}$. The utilized triple decomposition method does not guarantee explicitly that these are true. Let us check, therefore, how well they are satisfied.

Examination of the term $\langle u_i'' \rangle^l$ shows that this quantity is relatively small, though nonzero. The mean of its absolute value taken over the entire field of view equals roughly to 5% of the respective $u_{\mathrm{rms}}$ averaged over the same area (based on experiment 2). However, this statistic decreases with an increasing number of averaged velocity snapshots, which suggests its nonzero value is due to the convergence level (i.e., it equals to 8% of $u_{\mathrm{rms}}$ if only half of the total number of snapshots is used). It is also worth noting that $\langle u_i'' \rangle^l$ constitutes mainly high-wave-number, spatially unstructured noise. Its second Fourier coefficient, which is representative of wavelength $2\pi$, is relatively small.

Assumptions about $\overline{\tilde{u}_i^l \tilde{u}_i^m}$ and $\tilde{u}_i^l \tilde{u}_i^m$ are critical as they state that the utilized decomposition is energy preserving. An indication of the values reached by these correlations is given in Fig. 28. The plotted quantity is a maximum absolute value of a correlation taken over the entire field of view

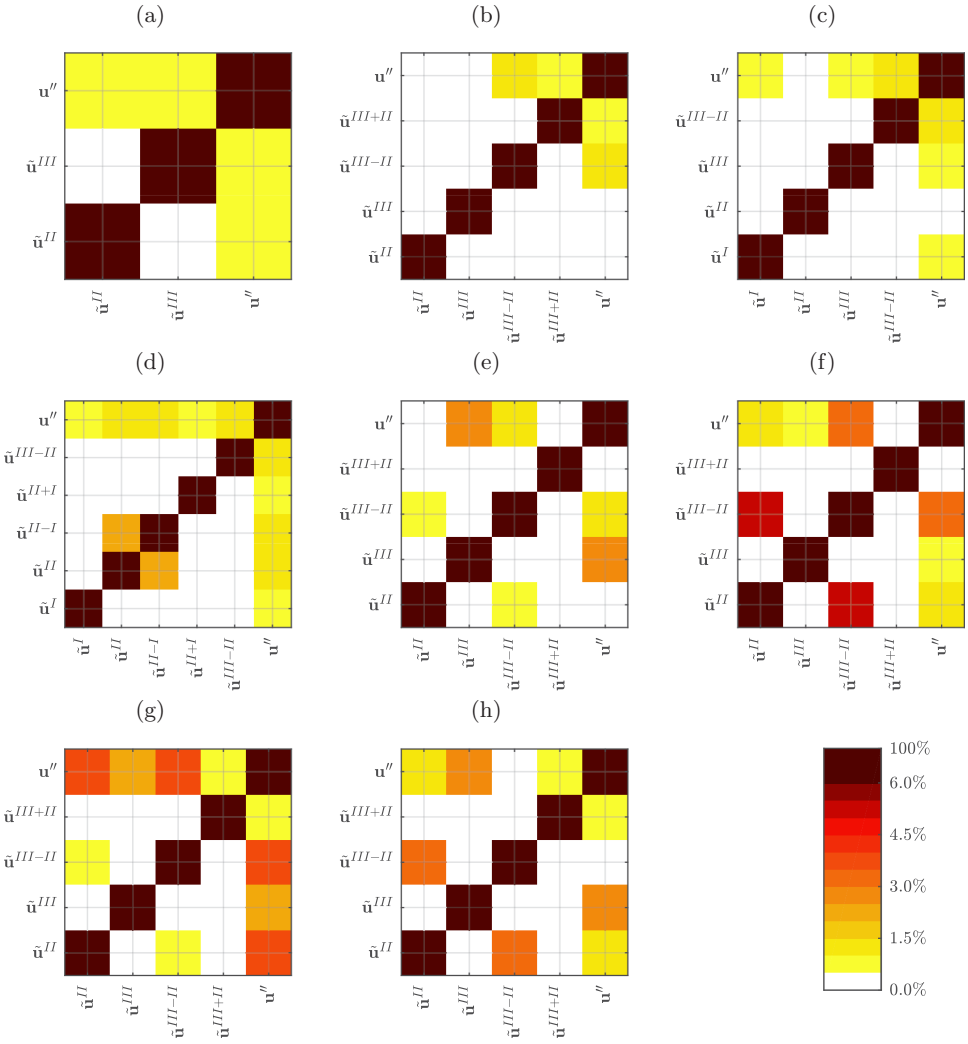


FIG. 28. Measurements the of correlations between different components of the velocity fluctuations, see (D1), evaluated based on data acquired from experiment 2 at $x/H =$ (a) 0.07, (b) 0.24, (c) 0.41, and (d) 0.57 and from experiment 3 at $(x/H, y/H) =$ (e) $(0.22, -0.34)$, (f) $(0.23, -0.26)$, (g) $(0.23, -0.35)$, and (h) $(0.36, -0.37)$.

(which is a rather conservative measure), i.e.,

$$\max_{\text{FoV}} \sum_i \left|\overline{\tilde{u}_i^l \tilde{u}_i^m}\right| \Bigg/ \left(\sum_i \overline{\tilde{u}_i^{l^2}} \cdot \overline{\tilde{u}_i^{m^2}}\right)^{1/2}. \tag{D1}$$

In the ideal situation, only the diagonal elements should be populated, which is not the case here. In both experiments 2 and 3, at all measured spatial locations correlations between stochastic and coherent fluctuations are nonzero. Fortunately, however, their values hardly reach 5%, and in most cases they fluctuate around 2% (it would be even less than 1% if the mean over a field of view, instead of the maximum, was considered). On the other hand, correlations between different coherent fluctuations are mostly zero. This is because a sufficient spectral separation of fluctuations (i.e., the respective spectral contents do not intersect) guarantees vanishing correlations. This is mostly the case, except for four situations. Within experiment 2, at the station $x/H = 0.57$, there is a residual

TABLE IX. The expected value (bias) and the rms value of the triple correlation terms' error due to the random measurement error $e$.

| Terms | Bias | Error r.m.s. |
|---|---|---|
| $\overline{\bar{u}u''u''}$ | $(\frac{e'_{\mathrm{rms}}}{u''_{\mathrm{rms}}})^2 \bar{u}u''^2_{\mathrm{rms}}$ | $2.0N_{\mathrm{aq}}^{-0.5}\frac{e'_{\mathrm{rms}}}{u''_{\mathrm{rms}}}\bar{u}u''^2_{\mathrm{rms}}$ |
| $\overline{\tilde{u}u''u''}$ | 0 | $2.0N_{\mathrm{aq}}^{-0.5}\frac{e'_{\mathrm{rms}}}{u''_{\mathrm{rms}}}\tilde{u}_{\mathrm{rms}}u''^2_{\mathrm{rms}}$ |
| $\overline{u''u''u''}$ | 0 | $5.2N_{\mathrm{aq}}^{-0.5}\frac{e'_{\mathrm{rms}}}{u''_{\mathrm{rms}}}u''^3_{\mathrm{rms}}$ |

correlation between coherent fluctuations $\tilde{\mathbf{u}}^{\mathrm{II}}$ and $\tilde{\mathbf{u}}^{\mathrm{II-I}}$. In the case of experiment 3, fluctuations $\tilde{\mathbf{u}}^{\mathrm{II}}$ and $\tilde{\mathbf{u}}^{\mathrm{III-II}}$ correlate to some extent at all considered spatial spots. Again, the values of the correlations are below 6%.

Although it is found that (6) are not exactly met within the studied data, the discrepancies are relatively small, of the order of 5%. Given the similar level of statistical uncertainty, this is a sufficiently close match to consider the assumptions (6) an acceptable approximation.

## APPENDIX E: UNCERTAINTY OF THE ENERGY BUDGETS' TERMS

The measurements' uncertainty has already been discussed in Sec. II; i.e., the measurement random error assessment is presented in Table II and the statistical convergence of some basic statistics are given in Table III. In order to check the uncertainty of the energy budget terms (8a) to (10a), let us acknowledge the fact that they can be written in a form of linear combinations of different velocity triple correlations, e.g., $\overline{u''_i u''_j \bar{u}_k}$, $\overline{\tilde{u}_i u''_j u''_k}$, etc. First, the uncertainty of their estimated values due to the random measurement error, assuming that the "true" values of $\bar{u}_i$ and $\tilde{u}_i$ are known (i.e., the sampling period is sufficiently long) is to be assessed. In such circumstances, the residual fluctuations $u'_i - \tilde{u}_i$ would contain both $u''_i$ and the random measurement error $e'_i$. The conservative uncertainty measures of the associated triple correlations, based on the error propagation method, are presented in Table IX. The bias can appear as a result of the noise self-correlation in the case of the term $\overline{\bar{u}u''u''}$; however, in the critical case (for $e'_{\mathrm{rms}}/u''_{\mathrm{rms}} = 18\,\%$; see Table II) it does not exceed 3 % of the term's expected value. The error rms values, on the other hand, decrease with $N_{\mathrm{aq}}^{-0.5}$, resulting in their negligible level (less than 0.5 % when compared to the associated scaling (i.e., $\bar{u}u''^2_{\mathrm{rms}}$, $\tilde{u}_{\mathrm{rms}}u''^2_{\mathrm{rms}}$, or $u''^3_{\mathrm{rms}}$).

The convergence estimation is more challenging. It is not clear in the context of the energy budget's components containing $\tilde{u}$ how to define the number of independent samples $N_0$ gathered in the acquisition process, and thus how to evaluate confidence intervals, as the coherent fluctuations are correlated for extremely long times. The number of independent measurements approximated

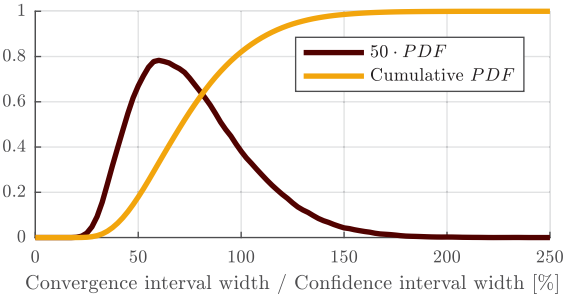


FIG. 29. PDF and the cumulative PDF of a ratio between the convergence interval and the confidence interval evaluated for a normally distributed random variable.

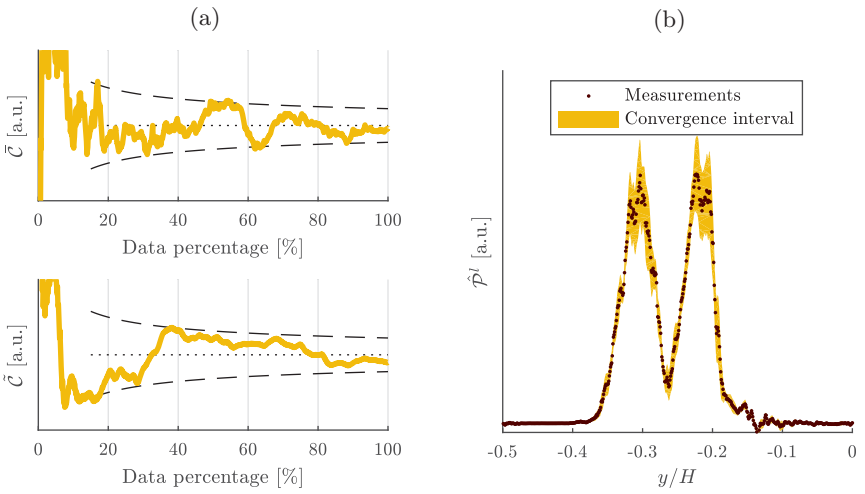


FIG. 30. Demonstration of convergence check: (a) evolution of 95% convergence intervals around converging convection terms of energy budgets and (b) the final convergence interval around a production term (based on experiment 2).

based on the integral time scale (see Table III) may not be representative here. In order to overcome this issue, a direct measure of statistical convergence of particular terms is proposed as an indication of the results' uncertainly. Let us define a 95% convergence interval $\mu \pm \sigma/\sqrt{N}$, which is the tightest possible interval that encloses 95% of the evaluations of a given statistic when calculated in a cumulative manner. Its final half-width $\sigma/\sqrt{N_{\mathrm{aq}}}$ stands as the convergence measure. Note that the half-width is inversely proportional to $\sqrt{N}$, which is in line with a definition of a confidence interval. The relation between the convergence interval and the classical confidence interval is

TABLE X. Critical values of half-widths of convergence intervals evaluated for different terms of the energy budgets at all the considered downstream locations, normalized with the maximum of the respective convection term (values given in percent, based on experiment 2).

| $x/H$ | Mode | $\bar{\mathcal{C}}$ or $\tilde{\mathcal{C}}$ | $\sum_l \tilde{\mathcal{P}}^l$ or $\tilde{\mathcal{P}}^l$ | $\hat{\mathcal{P}}^l$ | $\mathcal{P}''$ | $\tilde{\mathcal{T}}^l_+$ and $\tilde{\mathcal{T}}^l_-$ | $\bar{\epsilon}$ or $\tilde{\epsilon}$ | $\bar{\mathcal{D}}$ or $\tilde{\mathcal{D}}$ |
|---|---|---|---|---|---|---|---|---|
| 0.07 | $\bar{\mathbf{u}}$ | 3.8 | 2.0 | N/A | 1.1 | N/A | 0.0 | 2.9 |
| | $\tilde{\mathbf{u}}^{\mathrm{II}}$ | 4.2 | 12.3 | 4.0 | N/A | 0.3 | 0.0 | 13.3 |
| | $\tilde{\mathbf{u}}^{\mathrm{III}}$ | 4.7 | 16.4 | 3.3 | N/A | 0.2 | 0.1 | 14.7 |
| 0.24 | $\bar{\mathbf{u}}$ | 18.9 | 6.5 | N/A | 3.1 | N/A | 0.0 | 20.0 |
| | $\tilde{\mathbf{u}}^{\mathrm{II}}$ | 5.8 | 24.3 | 4.0 | N/A | 0.5 | 0.0 | 15.4 |
| | $\tilde{\mathbf{u}}^{\mathrm{III}}$ | 6.1 | 4.7 | 3.2 | N/A | 1.3 | 0.0 | 9.5 |
| | $\tilde{\mathbf{u}}^{\mathrm{III-II}}$ | 12.8 | 23.3 | 37.3 | N/A | 7.3 | 0.1 | 75.6 |
| | $\tilde{\mathbf{u}}^{\mathrm{III+II}}$ | 4.4 | 4.7 | 11.3 | N/A | 3.9 | 0.0 | 30.3 |
| 0.41 | $\bar{\mathbf{u}}$ | 10.0 | 3.8 | N/A | 2.1 | N/A | 0.0 | 7.8 |
| | $\tilde{\mathbf{u}}^{\mathrm{I}}$ | 7.6 | 25.5 | 4.1 | N/A | 1.1 | 0.0 | 35.0 |
| | $\tilde{\mathbf{u}}^{\mathrm{II}}$ | 7.9 | 7.3 | 4.2 | N/A | 0.6 | 0.0 | 21.6 |
| 0.57 | $\bar{\mathbf{u}}$ | 22.0 | 7.9 | N/A | 3.1 | N/A | 0.0 | 12.5 |
| | $\tilde{\mathbf{u}}^{\mathrm{I}}$ | 9.4 | 49.2 | 10.9 | N/A | 2.5 | 0.0 | 57.5 |
| | $\tilde{\mathbf{u}}^{\mathrm{II}}$ | 8.7 | 8.8 | 4.1 | N/A | 1.7 | 0.0 | 19.9 |
| | $\tilde{\mathbf{u}}^{\mathrm{II-I}}$ | 9.9 | 17.4 | 24.7 | N/A | 7.2 | 0.0 | 35.4 |
| | $\tilde{\mathbf{u}}^{\mathrm{II+I}}$ | 8.2 | 8.0 | 21.2 | N/A | 5.1 | 0.0 | 42.5 |

nontrivial. Figure 29 shows a PDF of the ratio between the two intervals evaluate for a normally distributed random variable. In most cases, the convergence interval is tighter; however, it can appear twice as wide in some cases. Figure 30(a) provides two examples of the appearance of convergence intervals evaluated for the mean and coherent convection terms.

The final convergence interval widths, if plotted on top of the energy budgets' curves in the form of error bars, would make the figures very busy and rather difficult to read [see Fig. 30(b) for an example]. In order to avoid this confusion, the half-widths of the convergence intervals are summarized in Table X, normalized with maxima of the respective convection terms.

[1] P. C. Valente and J. C. Vassilicos, The energy cascade in grid-generated non-equilibrium decaying turbulence, Phys. Fluids **27**, 045103 (2015).
[2] S. Goto and J. C. Vassilicos, Local equilibrium hypothesis and Taylor's dissipation law, Fluid Dyn. Res. **48**, 021402 (2016).
[3] G. Cafiero, S. Discetti, and T. Astarita, Heat transfer enhancement of impinging jets with fractal-generated turbulence, Int. J. Heat Mass Transf. **75**, 173 (2014).
[4] A. A. Verbeek, T. W. Bouten, G. G. Stoffels, B. J. Geurts, and T. H. van der Meer, Fractal turbulence enhancing low-swirl combustion, Combust. Flame **162**, 129 (2015).
[5] K. Goh, P. Geipel, F. Hampp, and R. Lindstedt, Flames in fractal grid generated turbulence, Fluid Dyn. Res. **45**, 061403 (2013).
[6] S. Weitemeyer, N. Reinke, J. Peinke, and M. Hölling, Multi-scale generation of turbulence with fractal grids and an active grid, Fluid Dyn. Res. **45**, 061407 (2013).
[7] S. Laizet and J. C. Vassilicos, Stirring and scalar transfer by grid-generated turbulence in the presence of a mean scalar gradient, J. Fluid Mech. **764**, 52 (2015).
[8] A. K. M. F. Hussain and W. C. Reynolds, The mechanics of an organized wave in turbulent shear flow, J. Fluid Mech. **41**, 241 (1970).
[9] B. Cantwell and D. Coles, An experimental study of entrainment and transport in the turbulent near wake of a circular cylinder, J. Fluid Mech. **136**, 321 (1983).
[10] R. Sonnenberger, K. Graichen, and P. Erk, Fourier averaging: A phase-averaging method for periodic flow, Exp. Fluids **28**, 217 (2000).
[11] R. Perrin, M. Braza, E. Cid, S. Cazin, F. Moradei, A. Barthet, A. Sevrain, and Y. Hoarau, Near-wake turbulence properties in the high Reynolds number incompressible flow around a circular cylinder measured by two-and three-component PIV, Flow, Turbul. Combust. **77**, 185 (2006).
[12] J. Bourgeois, B. Noack, and R. Martinuzzi, Generalized phase average with applications to sensor-based flow estimation of the wall-mounted square cylinder wake, J. Fluid Mech. **736**, 316 (2013).
[13] P. Baj, P. J. K. Bruce, and O. R. H. Buxton, The triple decomposition of a fluctuating velocity field in a multiscale flow, Phys. Fluids **27**, 075104 (2015).
[14] M. Couplet, P. Sagaut, and C. Basdevant, Intermodal energy transfers in a proper orthogonal decomposition-Galerkin representation of a turbulent separated flow, J. Fluid Mech. **491**, 275 (2003).
[15] Z. Hosseini, R. J. Martinuzzi, and B. R. Noack, Modal energy flow analysis of a highly modulated wake behind a wall-mounted pyramid, J. Fluid Mech. **798**, 717 (2016).
[16] A. K. Prasad, Stereoscopic particle image velocimetry, Exp. Fluids **29**, 103 (2000).
[17] M. Raffel, C. E. Willert, S. Wereley, and J. Kompenhans, *Particle Image Velocimetry: A Practical Guide* (Springer Science & Business Media, Berlin, 2007).
[18] R. Gomes-Fernandes, B. Ganapathisubramani, and J. C. Vassilicos, Particle image velocimetry study of fractal-generated turbulence, J. Fluid Mech. **711**, 306 (2012).
[19] C. Van Doorne, J. Westerweel, and F. Nieuwstadt, Measurement uncertainty of stereoscopic-PIV for flow with large out-of-plane motion, in *Particle Image Velocimetry: Recent Improvements* (Springer, Berlin, 2004), pp. 213–227.

[20] S. Herpin, C. Y. Wong, M. Stanislas, and J. Soria, Stereoscopic PIV measurements of a turbulent boundary layer with a large spatial dynamic range, Exp. Fluids **45**, 745 (2008).
[21] B. Wieneke, Stereo-PIV using self-calibration on particle images, Exp. Fluids **39**, 267 (2005).
[22] G. P. Romano, R. A. Antonia, and T. Zhou, Evaluation of LDA temporal and spatial velocity structure functions in a low Reynolds number turbulent channel flow, Exp. Fluids **27**, 368 (1999).
[23] L. Benedict and R. Gould, Towards better uncertainty estimates for turbulence statistics, Exp. Fluids **22**, 129 (1996).
[24] N. Mazellier and J. C. Vassilicos, Turbulence without Richardson-Kolmogorov cascade, Phys. Fluids **22**, 075101 (2010).
[25] A. Okajima, Strouhal numbers of rectangular cylinders, J. Fluid Mech. **123**, 379 (1982).
[26] D. Lyn, S. Einav, W. Rodi, and J.-H. Park, A laser-Doppler velocimetry study of ensemble-averaged characteristics of the turbulent near wake of a square cylinder, J. Fluid Mech. **304**, 285 (1995).
[27] S. C. Yen and J. H. Liu, Wake flow behind two side-by-side square cylinders, Int. J. Heat Fluid Flow **32**, 41 (2011).
[28] M. M. Alam, Y. Zhou, and X. Wang, The wake of two side-by-side square cylinders, J. Fluid Mech. **669**, 432 (2011).
[29] F.-L. Song, S.-Y. Tseng, S.-W. Hsu, and C.-H. Kuo, Gap ratio effect on flow characteristics behind side-by-side cylinders of diameter ratio two, Exp. Therm. Fluid Sci. **66**, 254 (2015).
[30] M. Kiya, H. Tamura, and M. Arie, Vortex shedding from a circular cylinder in moderate-Reynolds-number shear flow, J. Fluid Mech. **101**, 721 (1980).
[31] S. C. Yen and C. W. Yang, Flow patterns and vortex shedding behavior behind a square cylinder, J. Wind Eng. Indust. Aerodyn. **99**, 868 (2011).
[32] G. S. West and C. J. Apelt, The effects of tunnel blockage and aspect ratio on the mean flow past a circular cylinder with Reynolds numbers between 104 and 105, J. Fluid Mech. **114**, 361 (1982).
[33] M. M. Alam, M. Moriya, and H. Sakamoto, Aerodynamic characteristics of two side-by-side circular cylinders and application of wavelet analysis on the switching phenomenon, J. Fluids Struct. **18**, 325 (2003).
[34] J. Miau, G. Wang, and J. Chou, Intermittent switching of gap flow downstream of two flat plates arranged side by side, J. Fluids Struct. **6**, 563 (1992).
[35] Z. Wang and Y. Zhou, Vortex interactions in a two side-by-side cylinder near-wake, Int. J. Heat Fluid Flow **26**, 362 (2005).
[36] H. Kim, Investigation of the flow between a pair of circular cylinders in the flopping regime, J. Fluid Mech. **196**, 431 (1988).
[37] M. Hayashi, A. Sakurai, and Y. Ohya, Wake interference of a row of normal flat plates arranged side by side in a uniform flow, J. Fluid Mech. **164**, 1 (1986).
[38] P. Le Gal, I. Peschard, M. Chauve, and Y. Takeda, Collective behavior of wakes downstream a row of cylinders, Phys. Fluids **8**, 2097 (1996).
[39] D. Sumner, S. Wong, S. Price, and M. Paidoussis, Fluid behavior of side-by-side circular cylinders in steady cross-flow, J. Fluids Structures **13**, 309 (1999).
[40] N. A. Worth, T. B. Nickels, and N. Swaminathan, A tomographic PIV resolution study based on homogeneous isotropic turbulence DNS data, Exp. Fluids **49**, 637 (2010).
[41] G. I. Taylor, Statistical theory of turbulence, in Proc. R. Soc. London, Ser. A **151**, 421, (1935).
[42] W. K. George and H. J. Hussein, Locally axisymmetric turbulence, J. Fluid Mech. **233**, 1 (1991).
[43] K. M. Lam, P. T. Y. Wong, and N. W. M. Ko, Interaction of flows behind two circular cylinders of different diameters in side-by-side arrangement, Exp. Therm. Fluid Sci. **7**, 189 (1993).
[44] F.-L. Song, W.-T. Lu, and C.-H. Kuo, Interactions of lock-on wake behind side-by-side cylinders of unequal diameter at Reynolds number 600, Exp. Therm. Fluid Sci. **44**, 736 (2013).
[45] C. Morton and S. Yarusevych, Vortex shedding in the wake of a step cylinder, Phys. Fluids **22**, 083602 (2010).
[46] A. Wynn, D. S. Pearson, B. Ganapathisubramani, and P. J. Goulart, Optimal mode decomposition for unsteady flows, J. Fluid Mech. **733**, 473 (2013).

[47] F. A. Portela, G. Papadakis, and J. Vassilicos, The turbulence cascade in the near wake of a square prism, J. Fluid Mech. **825**, 352 (2017).
[48] L. W. B. Browne, R. A. Antonia, and D. A. Shah, Turbulent energy dissipation in a wake, J. Fluid Mech. **179**, 307 (1987).
[49] X. Liu and F. O. Thomas, Measurement of the turbulent kinetic energy budget of a planar wake flow in pressure gradients, Exp. Fluids **37**, 469 (2004).
[50] A. K. M. F. Hussain, Coherent structures and turbulence, J. Fluid Mech. **173**, 303 (1986).
[51] R. Gomes-Fernandes, B. Ganapathisubramani, and J. C. Vassilicos, The energy cascade in near-field non-homogeneous non-isotropic turbulence, J. Fluid Mech. **771**, 676 (2015).
[52] D. Hurst and J. C. Vassilicos, Scalings and decay of fractal-generated turbulence, Phys. Fluids **19**, 035103 (2007).
[53] P. Lavoie, G. Avallone, F. De Gregorio, G. P. Romano, and R. A. Antonia, Spatial resolution of PIV for the measurement of turbulence, Exp. Fluids **43**, 39 (2007).
[54] T. Tanaka and J. K. Eaton, A correction method for measuring turbulence kinetic energy dissipation rate by PIV, Exp. Fluids **42**, 893 (2007).
[55] J. De Jong, L. Cao, S. H. Woodward, J. P. L. C. Salazar, L. R. Collins, and H. Meng, Dissipation rate estimation from PIV in zero-mean isotropic turbulence, Exp. Fluids **46**, 499 (2009).